Thermal transport in chalcogenide-based phase change materials: a journey from fundamental physics to device engineering

Kiumars Aryana[1] *, *Cosmin Constantin Popescu*[2], *Hongyi Sun*[3,4], *Kiarash Aryana*[5], *Hyun Jung Kim*[1], *Matthew Julian*[6] *Md Rafiqul Islam*[7] *Carlos A. Ríos Ocampo*[3,4], *Tian Gu*[2,8], *Juejun Hu*[2,8], *Patrick E. Hopkins*[7,9,10]

[1]NASA Langley Research Center, Hampton, VA 23666, USA
[2]Department of Materials Science and Engineering, Massachusetts Institute of Technology, Cambridge, 02139, MA, USA
[3]University of Maryland, Department of Materials Science & Engineering, College Park, MD, USA
[4]University of Maryland, Institute for Research in Electronics & Applied Physics, College Park, MD, USA
[5]Department of Mechanical Engineering, Friedrich-Alexander-Universität Erlangen-Nuremberg, 91058 Erlangen, Germany
[6]Intellectual Ventures, Bellevue, WA, USA
[7]Department of Mechanical and Aerospace Engineering, University of Virginia, Charlottesville, Virginia 22904, USA
[8]Materials Research Laboratory, Massachusetts Institute of Technology, Cambridge, 02139, MA, USA
[9]Department of Materials Science and Engineering, University of Virginia, Charlottesville, Virginia 22904, USA
[10]Department of Physics, University of Virginia, Charlottesville, Virginia 22904, USA

Email Address: ka8bd@virginia.edu

Keywords: *Chalcogenides, Phase change memory, Thermal Conductivity, Reconfigurable Photonics*

Advancements in nanofabrication processes have propelled nonvolatile phase change materials (PCMs) beyond storage-class applications. They are now making headway in fields such as photonic integrated circuits (PIC), free-space optics, and plasmonics. This shift is owed to their distinct electrical, optical, and thermal properties between their different atomic structures, which can be reversibly switched through thermal stimuli. However, the reliability of PCM-based optical components is not yet on par with that of storage-class devices. This is in part due to the challenges in maintaining a uniform temperature distribution across the PCM volume during phase transformation, which is essential to mitigate stress and element segregation as the device size exceeds a few micrometers. Understanding thermal transport in PCM-based devices is thus crucial as it dictates not only the durability but also the performance and power consumption of these devices. In this paper, we review recent advances in the development of PCM-based photonic devices from a thermal transport perspective and explore potential avenues to enhance device reliability. We aim to provide insights into how PCM-based technologies can evolve beyond storage-class applications, maintain their functionality, and achieve longer lifetimes.

1 Introduction

Achieving dynamic control over the electrical, optical, and thermal properties of materials is a major technological endeavor that could usher in a new era of compact, low-power, and cost-effective technologies. In recent years, the emergence of metasurfaces and photonic integrated circuits (PICs) has sparked unprecedented interest across diverse industries[1, 2, 3, 4]. In this context, components that can actively modulate light via an external trigger serve as fundamental elements for

light routing and the advancement of photonic systems towards a compact and energy-efficient design[5]. To achieve this, materials with tunable optical properties could facilitate the on-demand manipulation of light in both phase and amplitude. This capability not only facilitates the storage and processing of data using optical signals but also enables the controlled manipulation of light for applications in free-space optics. The technological and scientific implications of materials with tunable optical properties could potentially drive substantial advancements in telecommunication[6, 7], information processing[8, 9], as well as biological sensing [10, 11] and imaging applications[12, 13].

Thus far, light modulation for compact devices and applications has been done either by mechanical components such as micro-electro-mechanical systems[14], or by electrical techniques such as thermo-optic effect[15], free carrier dispersion effects[16], and liquid crystals[17]. However, these approaches suffer from high power consumption, minimal changes in refractive index, and complex fabrication processes. Recent studies have shown that chalcogenide-based phase change materials (PCMs) are a promising alternative for manipulating light with unprecedented performance, multilevel tunability, and low power consumption, achieving levels as low as attojoules per cubic nanometer [18, 19, 20, 21]. This exceptional efficiency is due to the non-volatile nature of phase transformations in PCMs, which remain stable in a set phase without requiring an electric field, a characteristic often described as "set and forget". In addition to their outstanding energy efficiency, these solid-state PCMs have demonstrated remarkable durability in-memory applications, with the capability of up to $\sim 10^{12}$ switching cycles[22]. As a result of their large optical contrast, remarkable energy efficiency, and durability, they are considered an excellent material candidate for future reconfigurable optoelectronics. However, the main challenge in the integration of PCMs into functional devices is the high temperature required to trigger the phase transformation, which necessitates careful thermal management.

Table 1: Comparison of unique performance requirements for phase change materials in electronic memory devices, photonic integrated circuits (PICs), and free-space optics.

	Electronic	PICs	Free space
$\Delta\rho$	High importance	Low importance	Low importance
Δn	Low importance	Medium importance	High importance
Δk	Low importance	High importance	Medium importance
Switching Speed	<1 μs or >1 MHz	Application-specific	Restricted by thickness
Thickness	20 – 100 nm	20 – 30 nm	$\lambda/2\Delta n$
Thermal Conductivity	Lower the better	Low importance	Higher the better

This class of active materials initially emerged in rewritable optical disks and, due to their analogue (continuous) switching operation, quickly gained interest for integrating into the memory devices for the development of non-von Neumann computing architecture, specifically designed to mimic the human brain by storing and processing data within the memory cell itself[23, 24, 25, 26, 27, 28]. Very recently, with growing interests in photonic memory[8] and silicon photonics, the need for manipulating the optical signal on a chip scale dimensions has increased and propelled PCMs into new frontiers such as photonic switches[29], rewritable photonic circuits[30, 31], and photonic memory devices[32, 33]. More recently, with the integration of metasurfaces in functional devices such as flat optics and spectral filters, the applications of PCMs have transitioned into reconfigurable optics for free-space applications offering improved capabilities such as adjustable spectral filters[13, 34, 35], focusing lenses[36, 37, 38], and beam steering devices[39, 40, 41]. From a broad perspective, we categorize PCMs into three major groups based on their effective switching area, which varies according to their applications, as depicted in Fig. 1. For

memory applications and achieving higher storage density, a smaller switching volume on the order of sub-micron dimensions is preferred. For reconfigurable PICs, the effective switching size can range from a few microns to 100 microns, depending on the specific application. Finally, for PCMs used in free-space optics, it is essential that the effective switching area exceeds 100 microns[35]. Ideally, the thickness of the PCM for manipulating a free-space beam is given by $\lambda/2\Delta n$, which equates to 380 nm for a beam with a wavelength of 1550 nm. Thinner layers can be achieved using resonant structures, while thicker layers may be required if the refractive index contrast with the cladding is low. A general comparison of the unique performance requirements for PCMs across different applications is provided in Table 1.

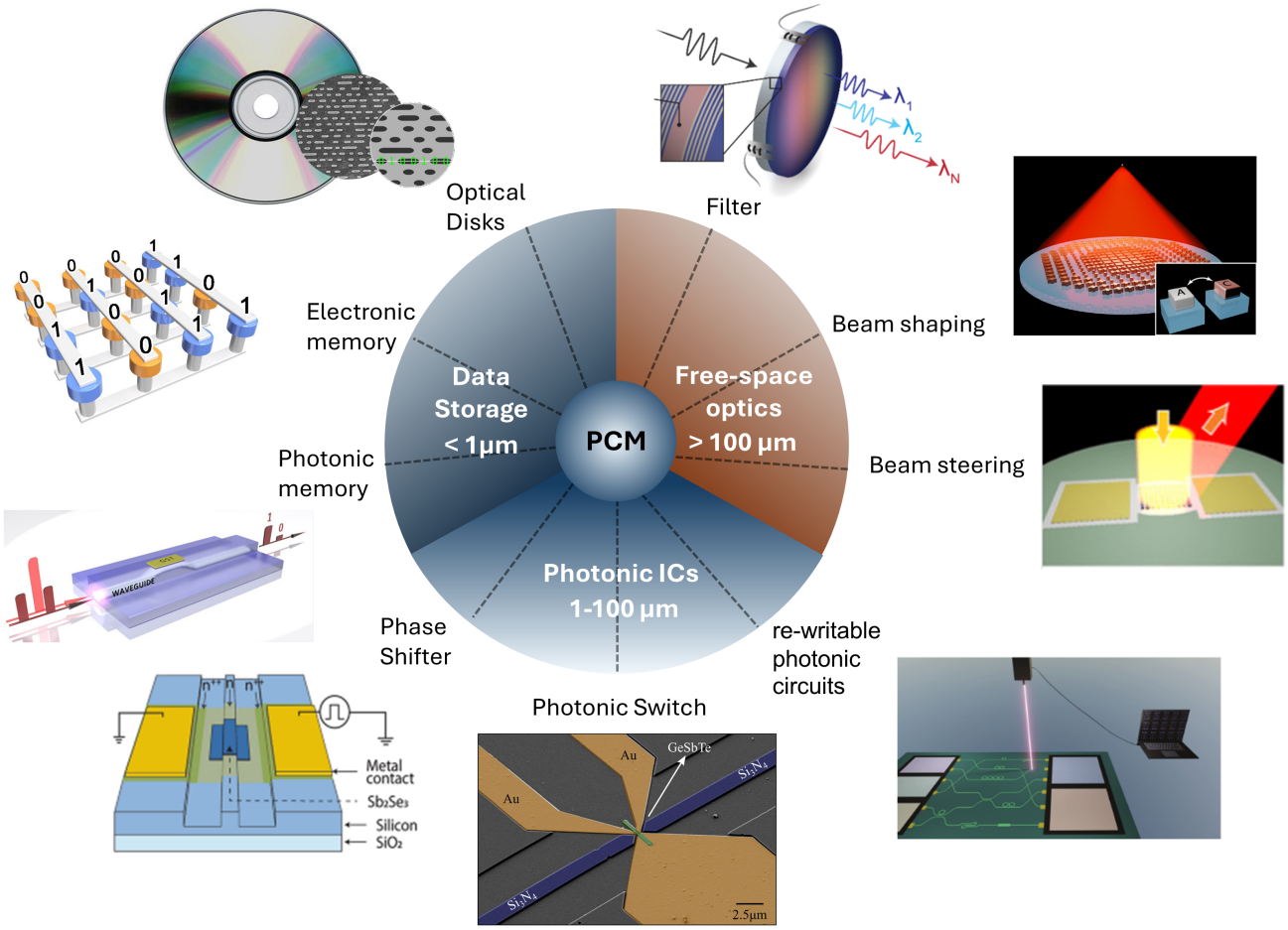

Figure 1: The application of phase-change materials in reconfigurable photonics can be categorized into three major groups based on their effective switching size: data storage (<1 μm), reprinted with permission Refs. [42, 43]. © 2015, Springer Nature. Photonic integrated circuits (1-100 μm), reprinted with permission from Refs. [44, 31, 45]. © 2022, Springer Nature. And free-space optics (>100 μm), reprinted with permission from Refs.[46, 36]. © 2021, Springer Nature.

As the application of PCM-based photonics expands, the reliability of these devices significantly lags behind their electronic counterparts. This is primarily due to the larger effective switching volume, which generates greater thermal shocks during the phase transformation process and requires a more robust device architecture to withstand them. For instance, switching the deposition technique for SiN_x from PECVD to sputtering has been shown to produce a hydrogen-free, stronger capping layer, thus improving PCM durability [47]. However, addressing durability issues

for large-scale PCM remains challenging and requires advancements at every level of the device. This paper explores the need for improvements in device architecture, material selection for better adhesion, innovative heater designs, and the development of PCMs with higher thermal conductivity and reduced volume changes during phase transitions to enhance reliability and durability.

This paper reviews recent advancements in PCM-based devices, with a specific emphasis on their applications in photonic and optoelectronic technologies. We explore strategies from a thermal transport perspective for improving device reliability and durability at dimensions larger than a few micrometers to facilitate the expansion of PCM-based devices into areas beyond conventional storage-class applications. Our discussion begins with a review of our current understanding of the thermal properties of PCMs and an analysis of their primary heat carriers, which are critical for temperature management within the device. We also discuss how thermal boundary conductance influences device performance and identify the length scale at which this factor becomes significant enough to affect the temperature distribution in PCM. Following this, we review recent microheater designs for PCM switching, assessing their effects on device efficiency and power consumption, while highlighting their benefits and limitations. Additionally, we review novel PCM compositions recently developed for photonic systems. Finally, we discuss computational methods for modeling phase transformations and summarize the reported thermal properties of major PCMs, which are crucial for effective thermal modeling.

2 Thermal Conductivity

Phase transformation in PCM causes drastic changes not only in electrical [48] and optical [8] properties, but also thermal conductivity [49], which can increase by more than an order of magnitude, as shown in Fig. 2(a-c). Since phase transformation in PCMs is triggered by thermal stimuli, an in-depth understanding of the thermal transport processes in PCMs and their interconnects is essential to expand their application beyond storage-class devices. This understanding would facilitate the development of larger PCM-based devices with more uniform phase transformation, which directly impacts the device's energy efficiency, performance, and durability. In this section, we focus on elucidating the critical thermal parameters that could affect device performance and lifetime as the effective switching volume in PCM increases. Through a systematic examination of energy carriers in different phases of PCM, we discuss the complex interplay of energy carriers, offering insights into the mechanisms governing heat transfer at the microscopic level.

The thermal conductivity of materials is largely affected by their atomic mass, atomic structure, and bonding nature. For example, carbon can naturally occur as either diamond or charcoal — one being exceptionally thermally conductive, while the other is insulating. Typically, the thermal conductivity of most materials ranges from 0.02 W m^{-1} K^{-1} for aerogels (over 99% porous) to a record high thermal conductivity for diamond exceeding ∼2000 W m^{-1} K^{-1} at room temperature [52, 53]. Although higher thermal conductivities than diamond have been reported for graphene [54, 55, 56] and carbon nanotubes (CNT) [57, 58], their large anisotropy in thermal conductivity and poor mechanical properties lead to major limitations for integration into functional devices [59, 60]. Figure 2(d) presents the thermal conductivity spectrum for various notable materials, ranging from super-insulative to superconductive. Figure 2(d) also highlights where the thermal conductivity of most PCMs falls within this range. According to this graph, PCMs are classified as low thermal conductivity materials, with their thermal conductivity being

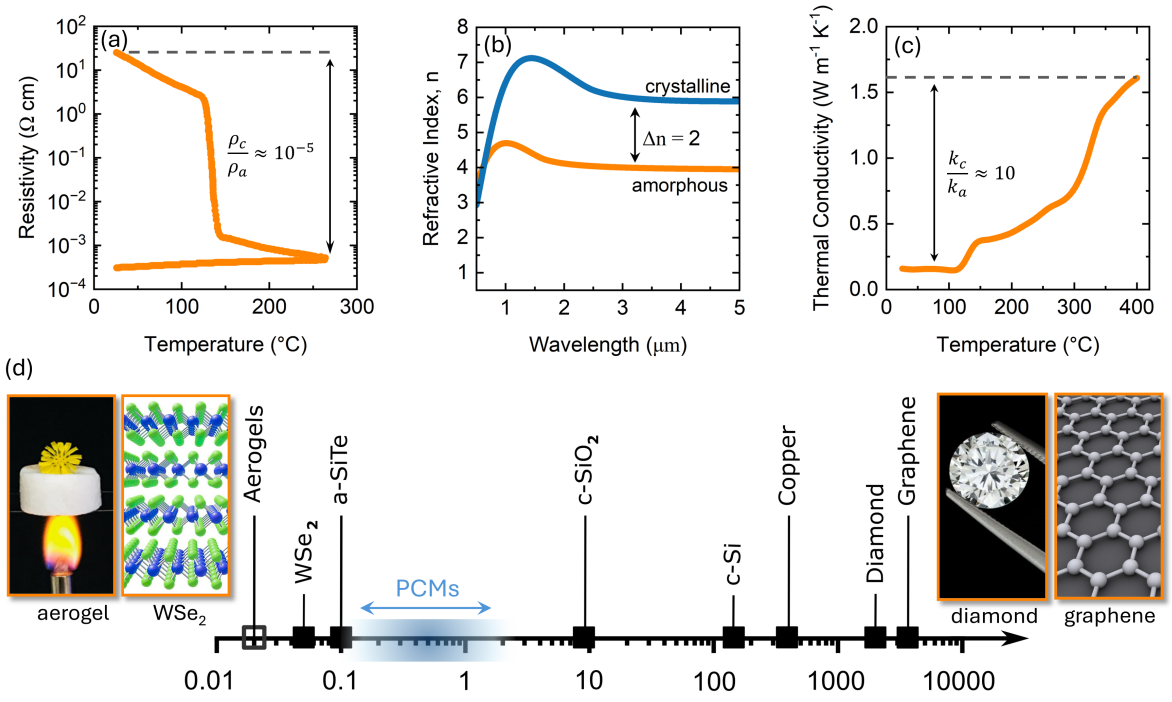

Figure 2: The changes in (a) electrical resistivity[50], (b) thermal conductivity[49], and (c) refractive index[51] upon amorphous to crystalline phase transformation in $Ge_2Sb_2Te_5$. (d) Thermal conductivity spectrum for several notable materials that are widely used in the industry from ultra-insulative to ultra-conductive.

comparable to that of polymers and amorphous silica (a-SiO_2). The low thermal conductivity of PCM results in a large temperature gradient during phase transformation, which becomes more pronounced as the PCM dimension increases. As we will discuss in this section, this temperature gradient could lead to elemental segregation and eventual failure of the device's performance over time.

2.1 Primary Heat Carriers in PCMs

Thermal transport is broadly categorized into three main mechanisms: conduction, convection, and radiation. In PCM-based devices, due to the high temperature excursions involved in phase transformation, the heater and PCM must be encapsulated with other inert, temperature-resistant materials such as SiO_2, ZnO_x, or SiN_x to prevent oxidation and evaporation. This necessitates that the PCM be fully enclosed by solid materials, making thermal transport predominantly driven by conduction, with convection and radiation having minimal impact on phase transformation and temperature distribution. The dominance of conduction arises from its significantly higher rate of heat transfer between two solids compared to the much lower rates associated with solid-air interactions or radiation. This can be quantified using a one-dimensional heat transfer model with a square heater adjacent to the PCM, encapsulated by a capping layer, as shown in the schematic in Fig. 3(a-c). The thermal conductance across solid-gas interfaces (convection coefficient) typically ranges from 2 to 25 W m^{-2} K^{-1}[61], while for solid-solid interfaces it is orders of magnitude higher, ranging from 20-300 $\times$ 10^6 W m^{-2} K^{-1}[62]. In addition, the radiation contribution compared to conduction is very small. We plot the heat transfer rate per unit area as a function of the PCM surface temperature in a steady-state regime in Fig. 3(d). Due to the significantly

lower thermal boundary resistance at solid-solid interfaces, heat transfer by conduction is almost six orders of magnitude higher than that by convection and radiation. This simplifies thermal transport in PCM-based technologies to a single mechanism, highlighting the importance of selecting appropriate materials for components near the microheater and the PCM. Consequently, the boundary condition at the interface between the encapsulating material and the air can be considered insulating, as depicted in Fig. 3(a).

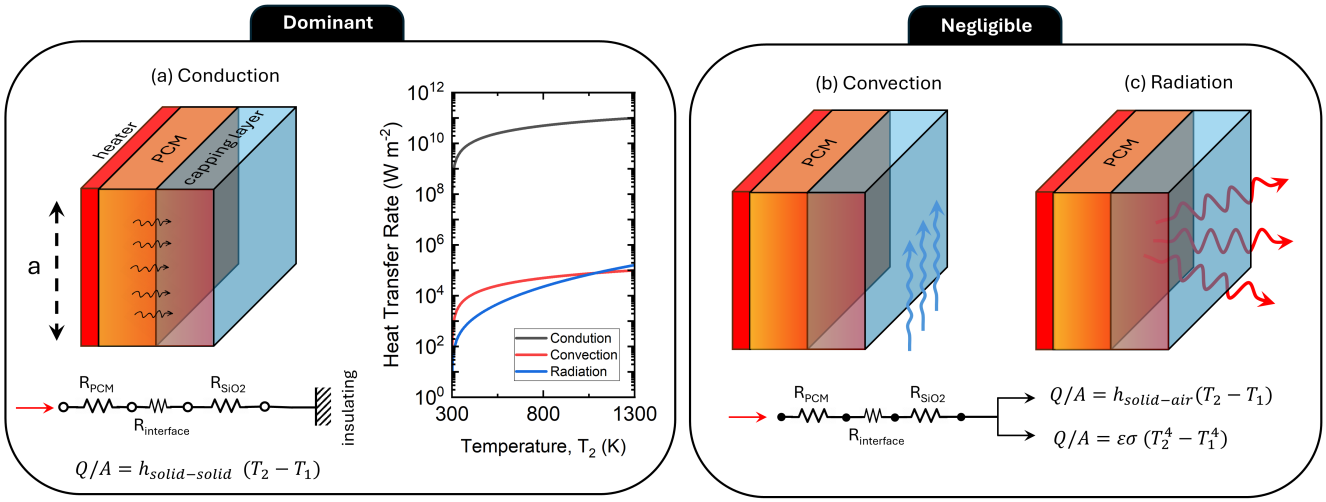

Figure 3: Different heat transfer mechanisms in PCM based devices are: (a) conduction, which is the dominant mode of thermal transport; (b) convection, and (c) radiation, both of which have negligible effects on thermal transport. Panel (d) shows the heat transfer rate for these mechanisms as a function of temperature.

Given that conduction is the primary mechanism of thermal transport in PCM-based devices, thermal energy in PCMs and its neighboring materials can only be transferred through two major pathways: (i) lattice contribution and (ii) electronic contribution. As a result, the total thermal conductivity of PCMs can be estimated by summing the contribution from vibrational modes in the lattice and the electrons to the thermal conductivity:

$$k = k_{\mathrm{l}} + k_{\mathrm{e}} \tag{1}$$

where k_{l} is the lattice contribution and k_{e} is the electronic contribution. Depending on the PCM atomic structure and composition, the contributions from vibrational modes and electrons to thermal conductivity can vary. These variations are rooted in the material's atomic structure and bonding nature, which strongly influence its electrical, optical, and thermal properties. In the amorphous state, the material exhibits covalent bonding with localized electrons, limiting electron mobility and resulting in high electrical resistivity. Upon crystallization, the bonding transitions to metavalent, characterized by delocalized electrons shared across multiple atoms in a coordinated lattice. This delocalization significantly enhances electron mobility, leading to a sharp reduction in electrical resistivity [63, 64, 65].

For instance, for the famous compound $Ge_2Sb_2Te_5$ (GST), the thermal conductivity in the disordered phase is mainly dominated by lattice vibrations with negligible contributions from the electrons, while in the highly ordered phase, the electrons become the dominant heat carriers[66, 49]. However, it is important to note that GST stands out as a PCM with exceptional transport processes. This is because, in addition to its structural phase transition near 150°C, it undergoes

a metal-insulator transition in its crystalline phase near 280°C due to vacancy reordering [67]. While in many other PCMs such as $Ge_2Sb_2Se_4Te$ (GSST) and Sb_2S_3 (SbS), thermal transport is mainly driven by lattice contribution in both phases[51]. In the following sections, we discuss how different heat carriers can influence the thermal transport in PCMs and its phase transformation.

2.1.1 Lattice Contribution

The thermal conductivity in non-metals, i.e. insulators and semiconductors, is governed by atomic vibrations, which are influenced by their mass, bonding, and structure[68]. At room temperature, energy transfer through atomic vibrations can be significantly more efficient than electronic transport. For instance, diamond, which is electrically insulative, has a thermal conductivity (>2000 W m^{-1} K^{-1}) more than five times higher than that of the most conductive metals, like silver (∼430 W m^{-1} K^{-1}) and copper(∼400 W m^{-1} K^{-1})[69]. At the same time, non-metals can also be among the most thermally insulating materials, such as layered tungsten diselenide, WSe_2 (∼0.05 W m^{-1} K^{-1}) and amorphous silicon telluride, Si_2Te_8 (∼0.10 W m^{-1} K^{-1})[70, 71]. Generally, materials with higher atomic mass, weaker bonds, and disordered structures exhibit lower thermal conductivities. As such, most chalcogenide-based PCMs that predominantly contain heavy elements like Ge, Se, Sb, and Te possess low thermal conductivities in both their amorphous and crystalline phases, often as low as 0.20 W m^{-1} K^{-1} in their amorphous phase, comparable to the thermal conductivity of polymers.

In crystals, heat is primarily carried by the collective motion of atomic vibrations, known as phonons, which is schematically depicted in Fig.4(a,b), which travel through the material at the speed of sound. Variations in atomic structure result in significantly different thermal conductivities and distinct temperature-dependent trends for the same material. For example, quartz (c-SiO_2) and silica glass (i.e., fused quartz or a-SiO_2) are composed of the same elements, but exhibit sharply contrasting temperature-dependent thermal conductivities, as illustrated in Fig. 4(c). This difference arises from the emergence of scattering mechanisms that impede the propagation of phonons as the atomic structure loses its periodicity and becomes less ordered. Beyond a certain degree of disorder, phonons are strongly scattered, and their mean free path becomes drastically short. As a result, in these highly disordered systems, the concept of phonons breaks down. This drastic change in the vibrational modes behavior at high atomic disorder necessitates the description of atomic vibrations through another concept known as "diffusons"[72], see Fig. 4(d,e). Diffusons are highly inefficient at carrying heat and are often strongly scattered within their first few nearest neighbors. This results in the lowest thermal conductivity that a material can achieve, a concept known as the minimum limit [73, 74]. Generally, the vibrational modes in amorphous solids are commonly classified into three categories based on their frequency: propagons, diffusons, and locons[75]. Propagons typically have lower frequencies and longer lifetimes compared to diffusons and locons. These vibrational modes can enhance the thermal conductivity of materials, but are generally found in single-element materials such as amorphous silicon[76, 77]. On the other hand, in disordered alloys where mass scattering and anharmonicity prevail and are more relevant to binary and ternary PCMs, diffusons are predominant energy carriers[74]. Locons are localized atomic vibrations that impede heat propagation, and as their population increases, thermal conductivity is suppressed. For example, in SiTe, increasing the Te concentration decreases the coordination number, resulting in 42% of the modes being locons, leading to ultralow thermal conductivities [71].

For non-metals, the thermal conductivity trend as a function of temperature is primarily dependent upon the degree of disorder in the atomic structure. For highly ordered single-crystalline

solids, the thermal conductivity decreases with temperature at temperatures close to room temperature and above. This is because as the temperature increases, more phonon modes are activated and this leads to the emergence of stronger phonon-phonon scattering, commonly referred to as anharmonic scattering [78]. On the other hand, for highly disordered materials, the thermal conductivity follows the trend of heat capacity and increases with temperature, as shown for amorphous SiO_2 in Fig. 4(c). This is because as the temperature of the materials is raised, more vibrational modes are activated, which can then contribute to the thermal transport. At the Debye temperature, when all vibrational modes are fully populated, the thermal conductivity plateaus and remains almost constant up to the crystallization or melting point [79]. In the case of most chalcogenide-based PCMs, due to their relatively soft bonding nature[80], this plateau occurs at temperatures well below room temperature. This implies that it is reasonable to assume a constant thermal conductivity for the amorphous phase of PCM above room temperature, before crystallization, which agrees well with prior measurements[66, 49, 51].

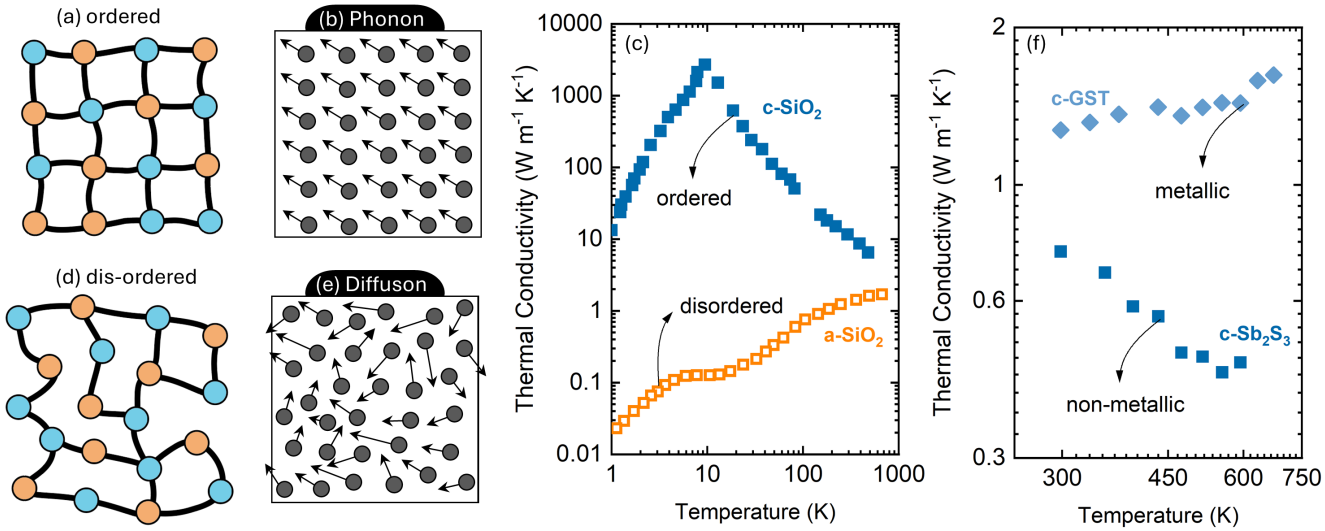

Figure 4: The dominant vibrational mode in PCMs is determined by their atomic structure: phonons (b) are the main heat carriers in ordered PCMs (a), whereas diffusons (e) dominate in disordered PCMs (d). Panel (c) shows the thermal conductivity trends with temperature for SiO_2 in both ordered and disordered states [81], and panel (f) presents these trends for metallic and non-metallic PCMs [49, 51].

Thus far we have discussed the heat carriers in non-metallic materials, where the heat is transported through atomic vibrations. However, depending on the composition of PCMs, the material can undergo a metal-insulator transition, causing the electronic contribution to thermal conductivity to become the dominant energy carrier in thermal transport. Figure 4(f) shows the thermal conductivity trend in crystalline GST and SbS with two differing behaviors. For crystals, the thermal conductivity typically decreases with temperature due to anharmonic scattering, as observed for c-SbS in Fig. 4(f), or remains constant in the presence of disorder or extrinsic scattering sites such as mass, grain boundaries, and defects [82, 83, 84, 85, 86]. However, for c-GST, since the thermal transport is dominated by electrons, it follows a metallic-like trend and increases with temperature. In the following, we discuss the effect of the electronic heat carriers in PCMs and discuss their impact on the overall operation of the device.

2.1.2 Electron Contribution

In conductive materials, the same particles that transport charge can also carry heat, and therefore, both electrons and atomic vibrations contribute to the thermal conductivity of the material. Electron-dominated thermal transport can significantly enhance temperature uniformity in a device for three main reasons: (i) increased overall thermal conductivity, (ii) an upward trend in thermal conductivity with rising temperature, and (iii) higher thermal conductivity in the liquid phase. In memory devices, it has been suggested that PCMs with lower thermal conductivity can reduce overall power consumption by confining heat more effectively [87, 88]. However, the impact of low thermal conductivity PCMs on improved power efficiency has been contested by others [89, 90]. Nonetheless, for scaling PCM applications to larger devices, higher thermal conductivity PCMs are advantageous. They facilitate a more uniform temperature distribution during phase transformation and reduce the required temperature rise at the electrode for triggering phase transformation [91].

For thin films, it can be challenging to distinguish the individual contributions of electrons versus vibrational modes [92]. The most common method to experimentally separate the contributions of electrons from vibrational modes is by measuring the electrical resistivity of the material, which can then be correlated with the thermal conductivity of electrons. The relative contribution of electrons to thermal conductivity can be estimated using the empirical Wiedemann-Franz (WF) equation, which relates electrical resistivity to thermal conductivity using a proportionality constant independent of the metal type [93]:

$$k_{\mathrm{e}} = LT/\rho \tag{2}$$

where k_e is the thermal conductivity of the electron, L is the Lorenz number, often assumed as the low temperature value of 2.44×10^{-8} W Ω K^{-2}, T is the temperature and ρ is the electrical resistivity Ω m. Using this approach, Lyeo et al. [66] reported a negligible electronic contribution to the thermal conductivity of GST in both the amorphous and crystalline phases when annealed up to 280°C. However, upon further annealing to 400°C, they observed that the electronic contribution could rise to as much as 70%. Similarly, Lee et al.[94] reported that the electronic contribution to thermal conductivity in GST is 0.87 W m^{-1} K^{-1}, accounting for 66% of the total thermal conductivity of 1.32 W m^{-1} K^{-1}. This sharp change in the thermal conductivity of GST in its crystalline phase was later discovered to be related to a metal-insulator transition (MIT) that occurs above 280°C as a result of the reordering of vacancies[67, 95]. This electronic phase transition is separate from the amorphous-to-crystalline phase transformation and occurs due to decreased randomness caused by the reordering of vacancies.

Nonetheless, the MIT does not occur in all PCMs even though it has been reported for the famous compound of Ge-Sb-Te[67] and GeTe[98], both of which go through crystallization upon early phase transformation and only by further annealing at higher temperatures, they transform into a metallic phase[99, 100, 101, 102]. Figure 5 (a) shows a schematic of the electronic density of states in GST in various phases, including the Fermi level and the mobility edge. In the amorphous phase, due to a high degree of disorder, the electrons are strongly scattered and localized, resulting in limited electron mobility and a bandgap of approximately 0.74 eV[96, 103]. Upon crystallization above 150°C, tellurium atoms quickly form an fcc sublattice, which creates a random arrangement of germanium, antimony, and vacancies within the sublattice[104, 105], as shown in Fig.5(b). This crystallization process creates a more ordered and periodic atomic arrangement, enhanced overlap of atomic orbitals, improved coupling, and more defined conduction

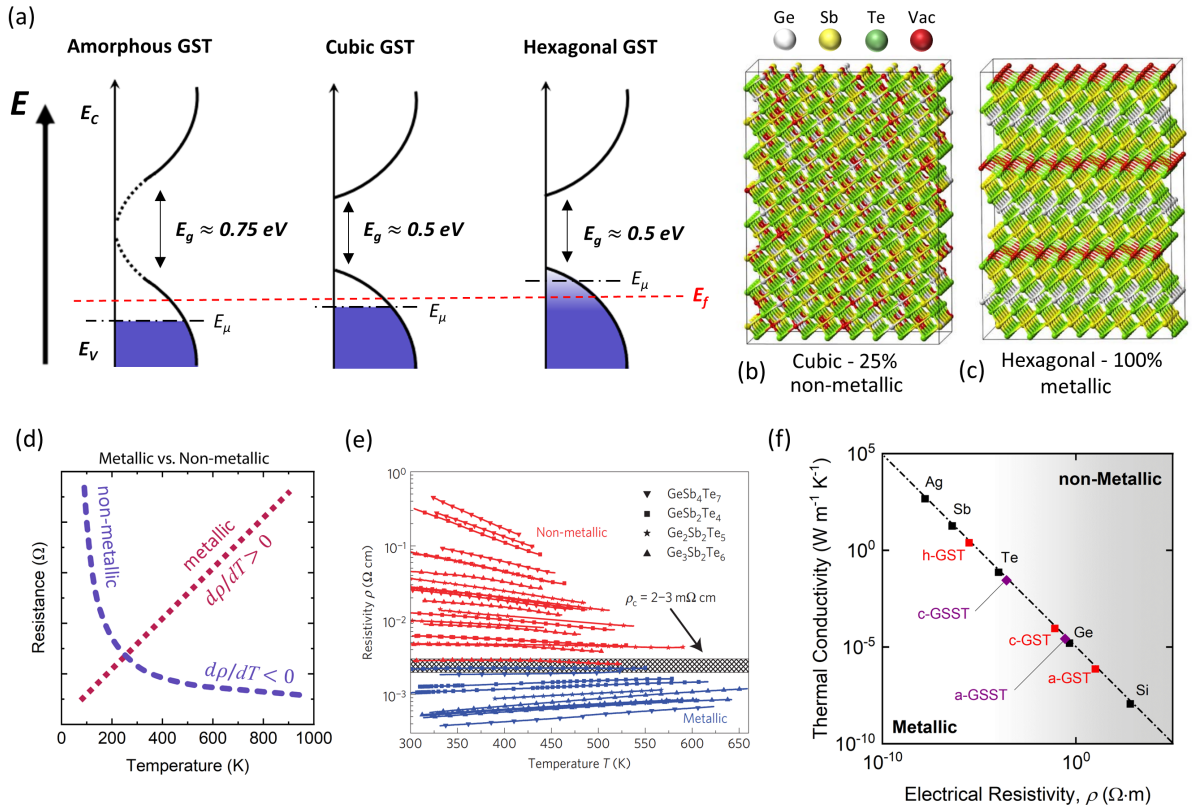

Figure 5: (a) A simplified schematic showing the electronic density of states of $Ge_2Sb_2Te_5$ in its amorphous, cubic, and hexagonal phases. E_μ and E_f are mobility edge and Fermi energy, respectively. Atomic structures of cubic (b) and hexagonal (c) GST, emphasizing the random distribution of atomic sites and vacancies. Reproduced with permission [95]. © 2012, Springer Nature. (d) Electrical resistivity trends as a function of temperature for metals and non-metals. (e) The change in electrical resistivity of $Ge_2Sb_2Te_5$ and the corresponding metal-insulator transition resulting from annealing at different temperatures. Reproduced with permission [67]. © 2011, Springer Nature. (f) Electrical resistivity of $Ge_2Sb_2Te_5$ in various phases compared to other materials [96, 97].

and valence bands, all contributing to the narrowing of the bandgap to 0.5 eV[96, 103]. Nonetheless, the random arrangement of the atomic sites in the sublattice leads to significant electronic localization, maintaining GST in the non-metallic insulating phase [67]. With further annealing of GST beyond 280°C, a higher degree of order is achieved in the lattice, Fig. 5(c), which enhances electron mobility and shifts the mobility edge above the Fermi level, as depicted in Fig. 5(a). This increased electron mobility leads to the formation of free electrons and triggers the metal-insulator transition (MIT) forming a degenerate semiconductor.

Figure 5 (d) shows a qualitative trend for the electrical resistivity as a function of temperature in metals (electron-dominated) and non-metals (phonon-dominated). In general, the electrical resistivity of metals increases with temperature while for non-metal it decreases. Figure 5 (e), we can observe that the electrical resistivity trend as a function of temperature changes as the annealing temperature increases for various compositions of Ge-Sb-Te[67]. This change in the electrical resistivity trend is an indication of MIT. Although we observe MIT in different compositions of GST as well as GeTe, most low-loss optical PCMs such as GSST, SbS, and SbSe do not exhibit metallic behavior in their crystalline phase, and their thermal transport is primarily dominated by vibrational carriers[106, 49, 51]. Figure 5(f) compares the electron thermal conductivity vs. electrical resistivity for GST, GSST, and some other notable metals and non-metals.

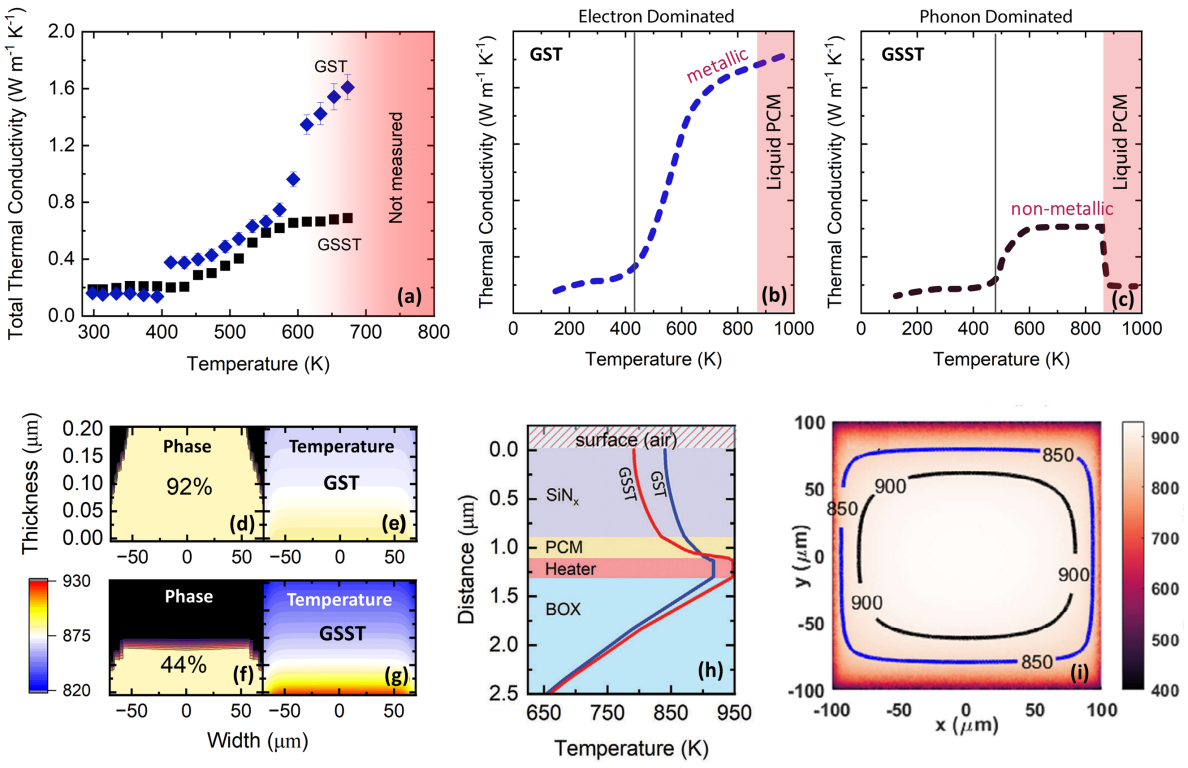

Figure 6: (a) Thermal conductivity data for GST and GSST, measured using TDTR, as a function of temperature. Reproduced with permission [49]. © 2021, Springer Nature. (b) A qualitative trend for the thermal conductivity of electron-dominated GST beyond its melting point. (c) A qualitative trend for the thermal conductivity of phonon-dominated GSST beyond its melting point [91]. (d,f) Degree of phase transformation under an identical amorphization pulse for similar devices equipped with GST and GSST [91]. (e,g) The corresponding temperature distribution during phase transformation. Reproduced with permission [91]. © 2023, Wiley-VCH GmbH. (h) Cross-plane temperature profile for a PCM/heater configuration when using GST and GSST as the PCM [91]. (i) Temperature distribution across the entire 200 μm × 200 μm region of the heater covered with GSST. Reproduced with permission.[35]. © 2024, Wiley-VCH GmbH.

For electron-dominated phase-change materials such as GST, the thermal conductivity sharply increases with temperature after the MIT above 280°C due to higher electronic contributions[66, 49]. This aligns with previous thermal conductivity measurements[66, 107], as shown in Fig. 6(a). Between 400°C and the melting temperature of 600°C, the electrical conductivity remains relatively constant until the solid-liquid phase transformation occurs. Near the melting point at 600°C, studies have observed a slight increase in the electrical conductivity of GST during the solid-liquid phase transformation [96, 108, 109, 110, 111]. Due to the challenges in measuring the thermal conductivity of liquid GST, experimental data for this phase are limited. However, we can make an informed estimate of the thermal conductivity trend during the solid-liquid phase transformation. Figures 6 (b,c) show a qualitative trend for the thermal conductivity of electron-dominated GST and phonon-dominated GSST. For electron-dominated GST, the electrical resistivity decreases upon melting, suggesting that the thermal conductivity will either increase or stay constant. On the other hand, in phonon-dominated GSST, the periodicity of the crystal breaks upon melting, and as a result, the thermal conductivity is expected to be closer to that of its amorphous phase. Figures 6 (dg) present simulation results that indicate the degree of phase transformation and the corresponding temperature distribution during the phase transition for a PCM/heater configuration when electron-dominated GST vs. phonon-dominated GSST is used[91]. According

to these results, with the same amount of applied heat, 92% of GST is amorphized, whereas only 44% of GSST undergoes amorphization. Furthermore, because the thermal conductivity of GSST is expected to decrease in the liquid phase, unlike GST, which increases due to higher electronic contribution, the heater must operate at a higher temperature when GSST is used as the PCM. Figure 6 (h) shows the cross-plane temperature profile of a device with PCM and an adjacent microheater, indicating that to amorphize the same volume, the heater for GSST needs to operate at nearly 31 degrees higher than for GST[91]. Additionally, Fig.6 (i) illustrates the temperature distribution for a 200 $\times$ 200 μm GSST on a silicon heater, highlighting the significant temperature gradients in the in-plane direction[35].

Although the observed increase in electronic contribution of GST agrees well with several independent reports, it could be difficult to conclusively determine its contribution percentage purely based on electrical resistivity data. A survey of the data available in the literature, as given in Table 2 for the electrical resistivity of GST annealed beyond 280°C reveals significant variations among the reported values for the electrical resistivity of GST, ranging by as much as an order of magnitude. For example, Bragaglia et al.[112] reported that the resistivity of hexagonal GST largely depends on the degree of order in the vacancy layers. They showed that for single crystalline h-GST, where the vacancy layers are highly ordered, the electrical resistivity could be substantially lower than reported values. This difference among the electrical resistivities could be partially due to the different deposition processes, composition variation, annealing time, or different measurement techniques. The first principle calculations demonstrate that the lattice thermal conductivity of the bulk h-GST can vary in the range of 0.87-1.67 W m^{-1} K^{-1} depending on the crystal orientation[113]. Similarly, using first principle calculations, Campi et al. [114] showed that by adding various scattering terms (Sb/Ge sublattice disorder and vacancies), the lattice thermal conductivity of bulk h-GST can be adjusted to reduce from an ideal value of $\sim$1.6 W m^{-1} K^{-1} to an experimentally reported value of $\sim$0.45 W m^{-1} K^{-1}. A more focused study on the effect of MIT on thermal conductivity can be found in ref. [106].

Table 2: Electrical resistivity for GST measured by different groups [96, 115, 94, 67, 66, 112] and the corresponding electronic contribution to thermal conductivity calculated from WF.

-	Resistivity h-GST (mΩ cm)	Measurement Temperature (°C)	Annealed Temperature (°C)	$Ge_2Sb_2Te_5$ Thermal Conductivity (W m^{-1} K^{-1})
Kato and Tanaka [96]	$\sim$3	100	580	0.2440
Nirschl et al. [115]	$\sim$2	100	350	0.3660
Lee et al. [94]	$\sim$0.84	25	300	0.87
Siegrist et al. [67]	$\sim$0.8	100	300	0.9150
Lyeo et al. [66]	$\sim$0.58	25	400	1.2513
Bragaglia et al. [112]	$\sim$0.32	0	270	2.2875

2.2 Thermal boundary conductance

At the interface between two solids, heat flow can be disrupted due to differences in physical properties such as atomic structure, adhesion, roughness, crystal orientation, and mismatch between the vibrational modes of the materials on each side. This disruption is quantified by thermal boundary conductance (TBC), which measures the rate of heat flow across an interface. The TBC is also often expressed as interfacial thermal resistance or Kapitza resistance—named after Soviet physicist Pyotr Kapitza [116]—describes the resistance to heat flow at an ideal, atomically perfect

interface [117]. However, in real-world devices, imperfections such as defects and surface roughness create a non-ideal interfacial region with a finite thickness, referred to as the Kapitza length. This theoretical length is an important parameter for quantifying the impact of thermal resistance on heat flow in relation to the bulk thermal conductivity. In the context of this paper, which examines a wide range of length scales for the PCM, the Kapitza length helps pinpoint the thickness at which TBC between PCM and its neighboring materials could significantly influence thermal transport. Thermal boundary conductance, often denoted as G, describes the relationship between the heat flux, Q, across the interface and the temperature drop, ΔT, at the interface, given by:

$$Q = \frac{\Delta T}{R} = G\Delta T, \tag{3}$$

where R is the resistance at the interface, the reciprocal of G. This conductance G is not an intrinsic property of the materials but is influenced by a combination of the electron and phonon properties of each material and the processes occurring in the interfacial region. Understanding TBC becomes essential when the characteristic dimensions of materials in PCM devices are comparable to or smaller than the Kapitza length. The Kapitza length is the thickness of a given material that would provide the same thermal resistance as the existing interface if it were to replace it and is defined by: [118, 119]:

$$L_k = k/(\text{TBC}), \tag{4}$$

where k is the thermal conductivity of the material. Kapitza lengths can range from nanometers for materials with low thermal conductivity, such as amorphous materials, to hundreds of micrometers for materials with high thermal conductivity. The Kapitza length in PCM reflects the trend in thermal conductivity and thus varies between amorphous and crystalline forms. For example, with a TBC of 50 MW $m^{-2}K^{-1}$, the Kapitza length for amorphous GST is approximately 4 nm, whereas for crystalline GST, it can extend up to 25 nm. This implies that for the amorphous phase, the GST thickness needs to be on the order of 4 nm to observe the effect of TBC, while for the crystalline phase, a GST thickness of around 25 nm would lead to a significant contribution from the thermal resistance at the interface.

In a device configuration, there may be numerous interfaces, some with previously measured TBC values and others for which experimental data is unavailable. For interfaces where TBC data are unavailable, an educated guess can be made based on the material properties. Although numerical models derived from the theory of phonon gases, such as the Acoustic Mismatch Model (AMM) and the Diffuse Mismatch Model (DMM), can provide estimates for TBC at low temperatures [117], they have been proven inaccurate for interfaces above room temperature [120, 121]. This is because the rate of heat transfer at the interface depends on parameters that can change during deposition, leading to deviations not only from numerical estimates but also from previously measured experiments. In this section, we offer insights into thermal transport at interfaces that are independent of the specific materials involved. These insights guide researchers in evaluating whether the TBC between two materials affects thermal transport and, if so, in approximating the TBC when experimental data are lacking.

Thermal energy at the interface between two solids can be transferred by electrons, phonons, or both. Electrons are more efficient at transporting heat across the interface, leading to the highest reported TBC values in metal/metal interfaces. For example, the TBC for Al/Cu interfaces is 4000 MW $m^{-2}K^{-1}$[122] and for Ir/Pd interfaces is 14000 MW $m^{-2}K^{-1}$[123], which are among the

highest measured TBCs. In contrast, phonons are much less efficient at transporting heat across interfaces, often resulting in a TBC nearly an order of magnitude lower. This inefficiency is the primary reason why diamonds, despite their exceptional thermal conductivity, do not achieve the expected performance when integrated with other materials in a device. Typical TBC values for phonon-dominated interfaces range from 20 to 300 MW $m^{-2}K^{-1}$ [124, 62]. Phonon-dominated TBC is more relevant to PCM-based devices, as most PCMs are found to be non-metallic. Prior measurements show that the TBC between GST and ZnS(80%):SiO_2(20%) composite increases from ∼60 MW $m^{-2}K^{-1}$ in the amorphous phase to ∼150 MW $m^{-2}K^{-1}$ upon annealing for 1 min at 250°C[125]. Since the annealing temperature is below the MIT temperature in GST, the change in TBC can only be attributed to the improved coupling of vibrational modes between the atomic vibrations on either side of the interface[126].

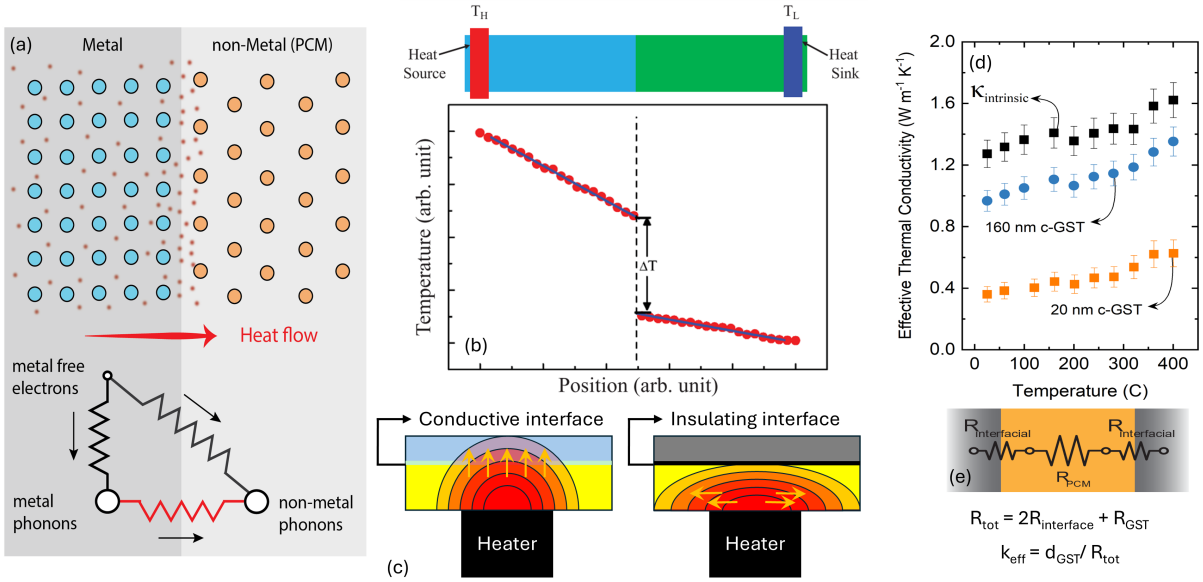

Figure 7: (a) Schematic of a metal/non-metal interface showing interactions between heat carriers, electrons, and phonons[127]. (b) Representative temperature profile across the interface between two different materials, reprinted with permission from Refs. [118]. © 2022, American Physical Society. (c) Qualitative comparison of temperature distribution and heat flow at an interface without and with an adhesion layer to enhance thermal transport [128]. (d) Effect of thermal resistance at the interface on the effective thermal conductivity of GST thin films at different thicknesses within a W/GST/W multilayer structure as a function of temperature [49]. (e) Schematic representation of thermal resistances for a thin film GST sandwitched between two tungsten layers.

In PCM-based electronic memory devices, heat typically transfers from a conductive electrode, such as tungsten or TiN, to the PCM. Depending on the length scale of the device components, the interfaces between the electrode, PCM, and their neighboring materials can affect the lifetime, performance, and power consumption of the device [129, 130, 131, 132]. It has been postulated that electron-phonon interactions at an interface can affect the heat transfer rate at a metal/non-metal interface [117]. Figure 7(a) shows the primary mechanism of thermal transport at an interface between a metal and a non-metal. In this case, heat is primarily transferred by electrons in the metal and, upon reaching the interface with a non-metal, transfer their energy to phonons at both sides of the interface. Depending on the efficiency of coupling between electrons and phonons, the TBC can change significantly. For instance, for the as-deposited amorphous GST/Ti interface, the TBC is reported to be 20 MW $m^{-2}K^{-1}$ and upon crystallization above 135 °C, it increases to 88 MW $m^{-2}K^{-1}$ [133]. Similar to the increase in TBC upon crystallization at the GST/ZnS:SiO_2 interface, this dramatic increase in TBC cannot be attributed to the MIT, as

the annealing temperature is below MIT (∼280°). A detailed investigation into the effect of phase transformation on the TBC for GST/W has shown that the TBC initially increases sharply upon crystallization to the rock-salt structure, and upon further annealing beyond 300°C, the TBC drops rapidly [107]. The primary reason behind this reduction, despite the increased contribution from electrons, remains unanswered. For the GST/W interface, the TBC does not change significantly between amorphous and 400°C annealed samples and only increases from 45 MW $m^{-2}K^{-1}$ to 55 MW $m^{-2}K^{-1}$ at room temperature.

Figure 7(b) shows a schematic of the temperature profile at an interface between two solids, illustrating a sharp temperature gradient due to disruption in heat propagation [118]. The temperature gradient at the interface can be manipulated to either increase or decrease the propagation of heat flow by adding an intermediate layer [134]. As depicted in Fig. 7(c) a conductive interface facilitates efficient heat propagation across the thickness of the PCM, resulting in a more uniform temperature distribution in the cross-plane direction. In contrast, an insulating interface causes the heat to spread laterally, potentially leading to a more uniform phase transformation in the in-plane direction. Thermal resistance at the interfaces was utilized to design heterostructure PCMs with enhanced reliability, durability, and reduced power consumption [135].

It is important to mention that the effect of TBC on thermal transport becomes significant as the dimensions of device components approach the length scales of carriers' mean free path. This is particularly relevant in memory devices and PICs where the PCM thickness could be less than 100 nm[107]. Typically, for devices with dimensions beyond several hundreds of nanometers, significantly larger than the carriers' mean free path, TBC does not play a major role and can be disregarded[136, 76, 107]. Figure 7(d) shows the effect of PCM thickness on its effective thermal conductivity as a function of temperature for 20 nm and 160 nm thicknesses, as well as its intrinsic thermal conductivity[107]. The effective thermal conductivity in this case encompasses all intrinsic and extrinsic scattering processes as well as the resistance at the interface. Based on this figure, the effective thermal conductivity for 20 nm PCM is more than a factor of three less than the intrinsic thermal conductivity of the PCM. At greater thicknesses, like 160 nm, the effect of interface on the overall thermal conductivity diminishes. Figure 7(e) presents a schematic of the resistance at the interfaces, which can be conceptualized as resistances in series. Resistance (R) is the inverse of TBC (1/TBC). This indicates that if one resistance in the series significantly increases relative to the others, the effect of the smaller resistances becomes negligible in determining the total resistance. Using this model, the total resistance of a GST layer sandwiched between two 5 nm W layers can be used to measure the effective thermal conductivity. Consequently, as the thickness of GST increases to several hundred nanometers, the effective thermal conductivity approaches the intrinsic thermal conductivity of GST.

The reduced thermal conductivity in the case of thin-film GST is not due to size effects or phonon-boundary scattering but is instead a result of pronounced TBC, which becomes more significant as the PCM thickness decreases. This thermal resistance at the interface can be leveraged to confine heat within the PCM boundaries and prevent heat loss. For example, in memory devices, it has been demonstrated that the reset current can be reduced by 90% by confining the heater electrode TiN in a thermal barrier TaN matrix with low thermal conductivity [137]. By incorporating a monolayer of 2D materials such as graphene [138] or MoS_2[139] between the PCM and the electrode, thermal leakage from the bottom electrode can be significantly mitigated, reducing the reset current by more than 40% and 70%, respectively. This improvement is due to the ultralow thermal conductivity of the 2D monolayer in the cross-plane direction, a result of its weak van der Waals interactions in the out-of-plane direction.

3 Suitable materials for microheater

In PCM-based devices, phase transformation is primarily triggered by either photothermal [140, 141, 142, 143] or electro-thermal [46, 144, 145] methods. Photothermal triggering usually involves a free space laser-writing setup or integrated high power fiber to PIC optical signal that allows switching via absorption of light by the PCM. Both of these methods require added complexity and potentially bulky components that preclude them from easy integration into many systems. Therefore, electrically triggering phase transformation is often preferred as it allows for a more compact integrated circuit design. We can identify two criteria for deposition of heat in the PCM electrically. First, there is the distinction between if the maximum current density, or main current path, occurs in the PCM or in an adjacent resistive element. This boolean can be rephrased as "Is the maximum power dissipation in the PCM?". Second, in the case of an adjacent resistive element, (i.e. the answer being no to the prior question), is that element metallic (i.e. optically non-transmissive) or a semiconductor (i.e. partially transmissive). The entire system is presupposed to use some adjacent conductive components to deliver the current during the heating process. In the case of PCMs integrated in systems such as phase change memories or photonic devices, the CMOS set of materials is typically leveraged, but some other materials can be integrated as well (e.g. graphene). While proof-of-concept integration of graphene in a 300 mm foundry process has been demonstrated, the growth and transfer requirements still require development before it will be feasibly provided by a commercial foundry, even though there are efforts to realize this goal [146].

3.1 Heating through the PCM in phase change memories

Focusing on the first criterion and presuming that the current passes through the PCM, this system basically describes phase change memories. These devices have been CMOS integrated and present a bottom and a top electrode in a layered structure. The PCM must reach temperatures above 600 ℃, so the list of viable conductive materials that are CMOS compatible and can withstand these temperatures is somewhat limited. Typical metals for CMOS would be W, Ti, Cu, Al and metals for silicides such as Mo, Ti, Ni, Co, [153, 154]. Al, for instance, would not be a good candidate as its own melting temperature is comparable to the one for GST. TiN has often been used as the intermediary before GST in phase change memories, in some cases as a diffusion barrier to prevent the formation of $TiTe_2$ [155]. Ag has been used in a recent design as part of a Ag/GST/HfO_2/Pt selector memory stack, with Ag diffusion into the GST being part of its operating mechanism [147]. Carbon nanotubes (CNT) can also be used in electrode materials, where the small gap in the CNT is filled with PCM and used in series and the resistive element [156, 157]. A strategy derived from the attempt to have lower switching energies in these systems is to confine the heat, leading to improved efficiency. As such, interfacial layers between the electrode and the PCM have been added to act as a thermal resistance barrier while aiming for as low an electrical resistance barrier as possible. Examples of such materials have been graphene, MoS_2, TiO_2, TiN, and WO_3 [138, 158, 159, 139, 160, 161].

3.2 Heating through adjacent resistive elements - photonics

The risk of optical losses typically restricts architectures that intersect metallic elements with the optical path, which inherently is the region requiring the PCM to switch. There have been several methods performed to circumvent these losses while allowing for sufficient heat dissipation. W-

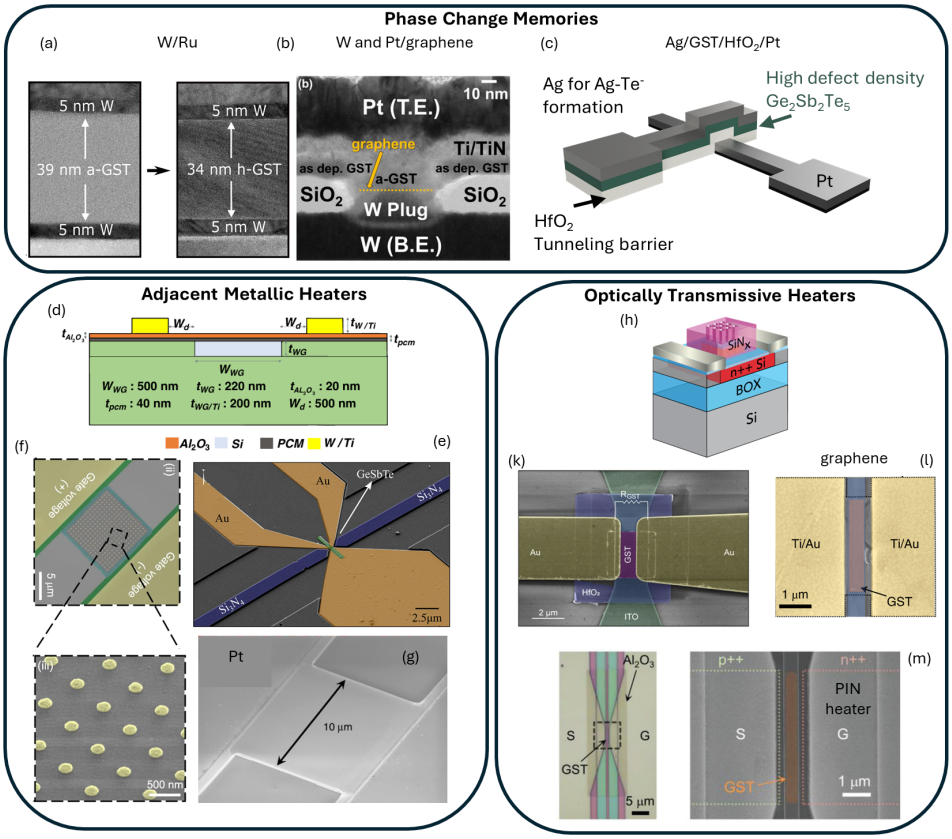

Figure 8: Examples of devices using the PCM as the heater element with metallic electrodes in phase change memory (a) Ru electrodes/W interface [107], (b) W + Pt electrodes with graphene thermal barrier [138], (c) $Ag/GST/HfO_2/Pt$ selector stack with Ag diffusion and AgTe formation as integral to device operation [147]) , using proximal metallic heaters (d) W heaters leveraging heat conduction through the substrate to prevent optical losse [148], (e) hybrid Au/GST PCM photonic device, where the plasmonic behavior of the Au heaters is desired [44], (f) W heater with Au/GST stack free-space reflective metasurface [149], (g) Pt heater for reflective GSST metasurface [150], and transmissive heaters (h) thick GSST metasurface on near-IR transmissive doped Si heater [35],(k) Au electrodes with an ITO heater for a GST PCM element on a waveguide (Reprinted with permission from [151], ©Optica Publishing Group) ,(l) graphene-based heater with Ti/Au electrodes for GST-based PIC [21], (m) PIN junction heater, driving the inherent heater losses lower for a GST-based PIC (Reprinted with permission from [152] ©John Wiley and Sons).

Ti side microheaters placed nearby the waveguide, leveraging in-plane heat dissipation have been used, with W again being highlighted for its superior thermal resilience (Fig. 8 (d)) [148]. This type of design would require materials that tolerate temperatures even above the melting point (T_m) of the PCM as the distance from heater to the PCM will result in a drop in temperature that needs to be balanced against. In doped Si heaters, platinum has also been leveraged with similar considerations (Fig. 8 (g)), while gold was used when lower thermal endurance could be tolerated [162]. Between gold, platinum and tungsten, the former has a higher reflectivity and optically could be the desired metal (depending on the targeted optical output) but Pt and W have superior thermal resilience. Although metallic structures are typically used in reflection, due to the short optical absorption length, they could be designed for a transmissive application, as seen in Fig. 8 (e) [44]. Still, the low transmission values may require a change in design or trading the mixed output mode of the device.

Up to this point, we highlighted the metals used in the electrical connection but the materials

that deposit heat closest to the PCM can be also relatively transmissive structures such as doped Si and PIN diode heaters [163, 45, 164, 165, 152], graphene [19, 21], and ITO [151, 166], which allow for direct contact with the PCM without entirely absorbing the optical signal. These materials can be leveraged, but inherent limitations and trade-offs between size, required voltage and power, and optical performance will always occur, as a more conductive system is typically more absorptive, limiting transmission and Q-factors, critical performance metrics in optical devices. Meanwhile, lower electrical conductivity systems may limit the switching area or require the application of larger electric fields to compensate for potentially improved optical performance. PIN heaters have the potential to provide the best of both worlds for integrated PCM photonics, as they are CMOS compatible (no custom steps need to be incorporated), avoid dopants in the waveguide area and can reach the desired temperatures. A scale-up to larger PIN structures for free-space applications would be an important step forward for lower-loss free-space PCM photonics.

2D microheaters. Since the discovery of graphene through exfoliation of graphite in 2004[167], great efforts have gone into the integration of this exotic 2D material into high-speed electronic and photonic devices. The graphene flexibility, scalability, low heat capacity, compatibility with CMOS fabrication, and its large anisotropy in thermal conductivity make it an ideal candidate for application as a microheater in PCM-based devices to improve performance and mitigate power consumption. The anisotropy in the thermal conductivity of graphene is related to its high in-plane bonds and weak Van der Waals interaction in the cross-plane direction, which leads to more than 5 orders of magnitude difference between its in-plane and cross-plane directions. Graphene was first used in phase change memory devices to address the problem of thermal leakage using its ultra-low cross-plane thermal conductivity. This property originates from the weak Van der Waals interaction between the graphene layers and adjacent layers, leading to a very low TBC, which proved to be effective in improving thermal leakage from the bottom electrode in PCM devices[138]. The separation in Van der Waals forces between graphene layers is reported to be 0.335 nm, and the experimentally measured thickness of graphene could vary from 0.4 to 1.7 nm[168, 169]. Considering a thickness of 1 nm for graphene and a TBC of 25 MW $m^{-2}K^{-1}$[170], we can estimate the effective cross-plane thermal conductivity of a single layer of graphene to be approximately 0.025 W m^{-1} K^{-1}, as shown in Fig. 9(a), which is comparable to the thermal conductivity of air. Due to such low thermal conductivity, graphene can effectively be used as a thermal barrier in PCM-based devices. On the other hand, graphene is extremely conductive along the lateral direction within its layer. The thermal conductivity of suspended single-layer graphene is reported to be on the order of 2500-5300 W m^{-1} K^{-1}[54, 171], while the thermal conductivity of supported graphene on SiO_2 has been reported to be 370-600 W m^{-1} K^{-1} [172, 171]. This dramatic reduction in the in-plane thermal conductivity is the result of phonon-substrate scattering and is a more accurate representation of graphene's in-plane thermal conductivity in the device configuration. Given the single atomic layer of graphene, this value is still higher than that of the most conductive metals, such as silver, which has a bulk thermal conductivity of 429 W $m^{-1}K^{-1}$ at room temperature [173].

Recently, there has been a growing interest in using graphene as a microheater to trigger phase transformation in PCM-based devices, particularly for application in PICs. Graphene's low heat capacity enables ultra-low power consumption, and its high in-plane thermal conductivity allows for a more uniform temperature distribution, leading to more uniform phase transformation. Graphene was first used as a heater to switch exfoliated In_2Se_3 with set and reset voltage of 0.7 V and 3 V, and pulse duration of 50 ns and 70 μs, respectively [174]. Rios et al. [19] integrated graphene and GSST to replace volatile electro-thermal modulation of waveguides as shown in Fig.9(c), demonstrating that graphene not only outperforms metallic heaters with lower insertion losses (0.03-0.05 dB) but also achieves reliable phase transformation with exceptionally low power consump-

tion—8.6 mW for amorphization and 5.5 mW for crystallization. The authors estimated the TBC between graphene and the SiO_2 layer using the minimum pulse needed to trigger amorphization (melting PCM) and found it to be approximately 0.18 MW $m^{-2}K^{-1}$, nearly two orders of magnitude lower than the TBC reported in the previous paragraph. However, graphene corrugation has been shown to lead to a significant variation in measured TBC, ranging from 0.001 MW $m^{-2}K^{-1}$ for suspended graphene to 100 MW $m^{-2}K^{-1}$ for a fully contacted graphene/substrate interface [175]. In addition, graphene has recently demonstrated record breaking switching energy density on the order of attojoule (8.7 aJ nm^{-3})[21]. Figures 9(e,f) show a graphene microheater integrated in a microring resonator to switch Sb_2Se_3 between its amorphous and crystalline states, thereby controlling the phase of light traveling through an optical waveguide[21]. This method achieved a maximum resonance shift of 0.021 nm (0.00822π) at 1549 nm, as shown in Fig. 9(g), and demonstrated excellent endurance with reversible switching over 1000 cycles, Fig. 9(h).

Non-2D (bulk) microheaters. One of the early implementations of doped Si for PCMs leveraged ITO electrodes as well, and had the intended current path through the GST layer (Fig. 10 a). Future designs have taken the benefits of ITO and doped Si but attempting for larger modulations by passing the current through nearby elements[163]. Alternating PIN junctions allow for bidirectional operation of heating/switching units, as one pair in the system dissipates heat in forward bias while the adjacent one is not-switched due to being in reverse bias (Fig. 10 b). Optimization of this design can decrease the footprint of PCM-based PICs [179]. By engineering the position of the dopants in the Si layer, the position of the hot spots can be controlled such that we can deliberately switch only a fraction of the PCM layer in a more controlled manner (Fig. 10 c) [180]. Some PCM-PIC designs (based on Sb_2S_3 in this case) used the electricaly conductive ITO layer also as a blanket protector of the PCM, with the possible advantage of a simpler fabrication process, as both materials can be sputtered sequentially, without breaking the vacuum (Fig. 10 d) [181]. Subsequent designing with ITO have investigated the potential of tunable Bragg reflectors using low loss PCMs such as with Sb_2Se_3 (Fig. 10 e) [182]. An important development in PIC PCM designs originates in thermo-mechanical considerations of thermally induced stress in the comprising layers (Fig. 10 f). By depositing the PCM, heater and protective layer in a recessed area, improved reliability and lower stresses at the heater and PCM interface were observed [183]. Various metal heater designs have been proposed, such as surface plasmon polariton ones (Fig. 10 g), mixing the benefits of non-volatile contrast of PCMs with the small footprint enabled by plasmonics [184], as well as aiming to operate the PIC via dielectric means only, with the metal components being well separated from the waveguide (Fig. 10 h). Due to the thermal overeshooting needed for metal designs, quench times may still be superior in PIN heaters [185]. Optimizations of the metal heater-based PCM PIC designs are ongoing. Simulations of Ti/TiN heaters show that a distance of 200 nm is sufficient for negliable loss from the metal heater, informing design consideration, even when accounting for thermo-optic variations of the metal (Fig. 10 i) [186]. Potential hybrid heaters can be envisioned, such as large doped Si with ITO cladding on top, allowing for bidirectional heating and thus potentially larger switching volumes, but this will come with the required thermo-mechanical considerations of the stresses and strains induced in each layer. Similarly, a design that could be allowed in a typical commercial foundry is a metalic + doped Si or PIN heater, assuming the required distances to the metal layer are accounted for. These hybrid designs may allow for more flexibility and uniform heating of the PCM layer or for increased complexity. It is noted that a lot of PCM designs require the deposition of the PCM after the front-end of the line but before the SiO_2 deposition and planarization, which will require reliable integration of these materials in typical commercial foundries.

The successful integration of transparent graphene heaters into reconfigurable photonic circuits has inspired further exploration of graphene/PCM as an effective method for creating electro-

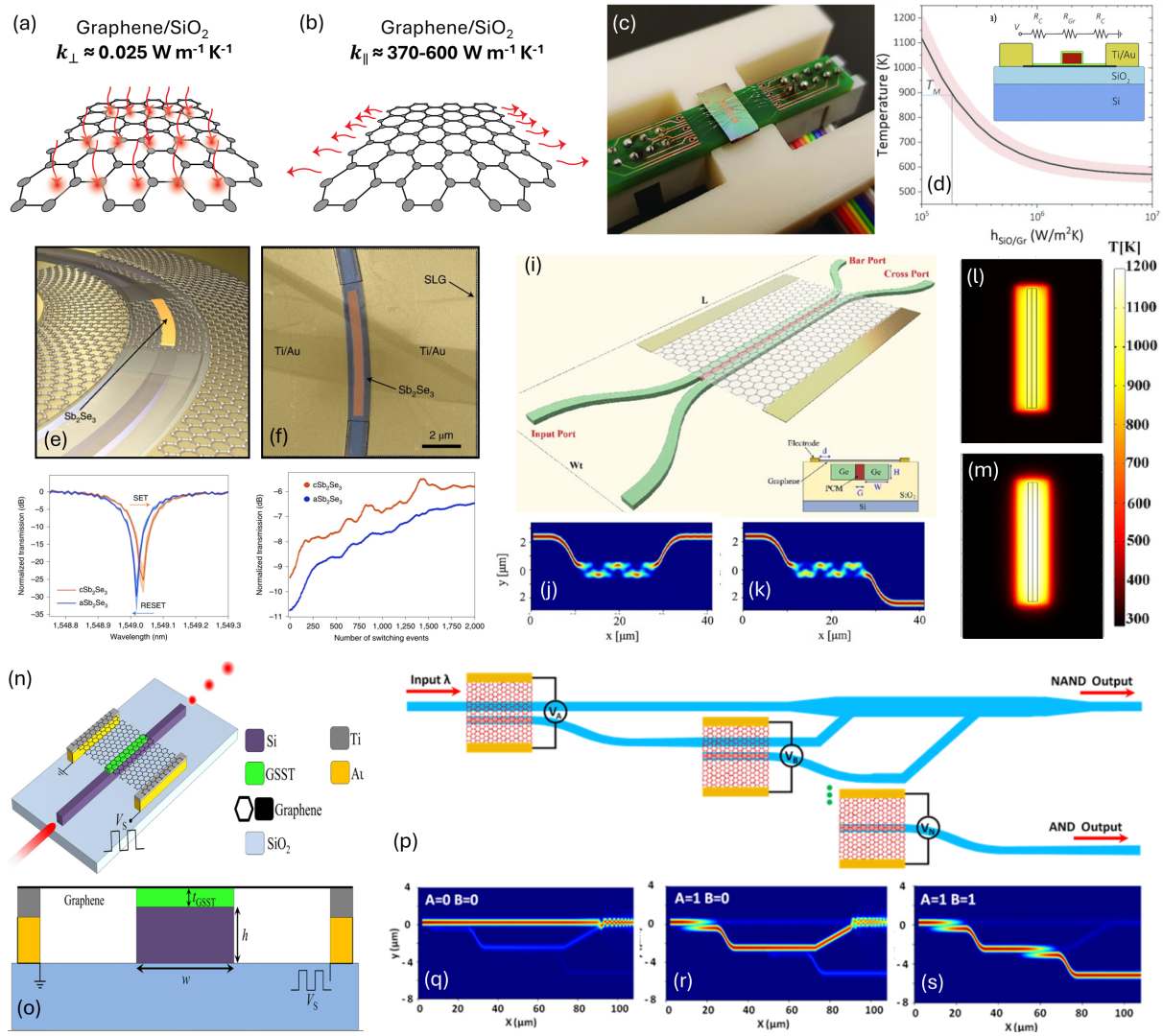

Figure 9: Thermal conductivity of graphene on SiO_2 in the (a) cross-plane and (b) in-plane direction. (c) Image of a graphene-integrated photonic chip attached to a custom PCB with wire bonds and (d) maximum temperature at the interface between graphene and PCM as a function of its TBC, reprinted with permission from Ref. [19]. © 2020, Wiley-VCH GmbH. (e,f) 3D illustration and false-colour SEM image of a phase shifter featuring graphene and Sb_2Se_3 integrated into a micro-ring, and (g) the corresponding resonance wavelength shift during phase switching of the PCM between amorphous and crystalline states at 1549 nm in the micro-ring, with (h) the durability of the graphene heater demonstrated through cycling of Sb_2Se_3. Reprinted with permission from Ref. [21]. © 2022, Springer Nature. (i-m) Waveguide coupler equipped with low loss Sb_2Se_3 and a graphene heater for operation in mid-IR. Reprinted with permission from Ref. [176]. © 2024, Elsevier Ltd. (n,o) 3D illustration and cross-section view of the proposed GSST-based waveguide with graphene microheater. Reprinted with permission from Ref. [177]. © 2023, Elsevier Ltd. (p-s) Schematic of the proposed non-volatile directed logic circuits with GSST and graphene microheater. Reprinted with permission from Ref. [178]. © 2023, IEEE.

optical switches in photonic circuits. Through computational models and simulations, as shown in Figs. 9(i-m), Soref et al. [176] proposed a multi-level electro-optical switch utilizing Sb_2Se_3 as the active material for mid-infrared operation on a germanium-on-insulator platform. This switch features an active coupling length of 17 μm, operates over a 30 nm bandwidth, and exhibits insertion losses of less than 0.3 dB. Pouyan et al. [177] introduced a GSST-based Mach-Zehnder modulator with an active length of 4.725 μm, an insertion loss of less than 2 dB at 1550 nm, and a suspended graphene heater to enhance switching speed and efficiency. Similarly, it has been

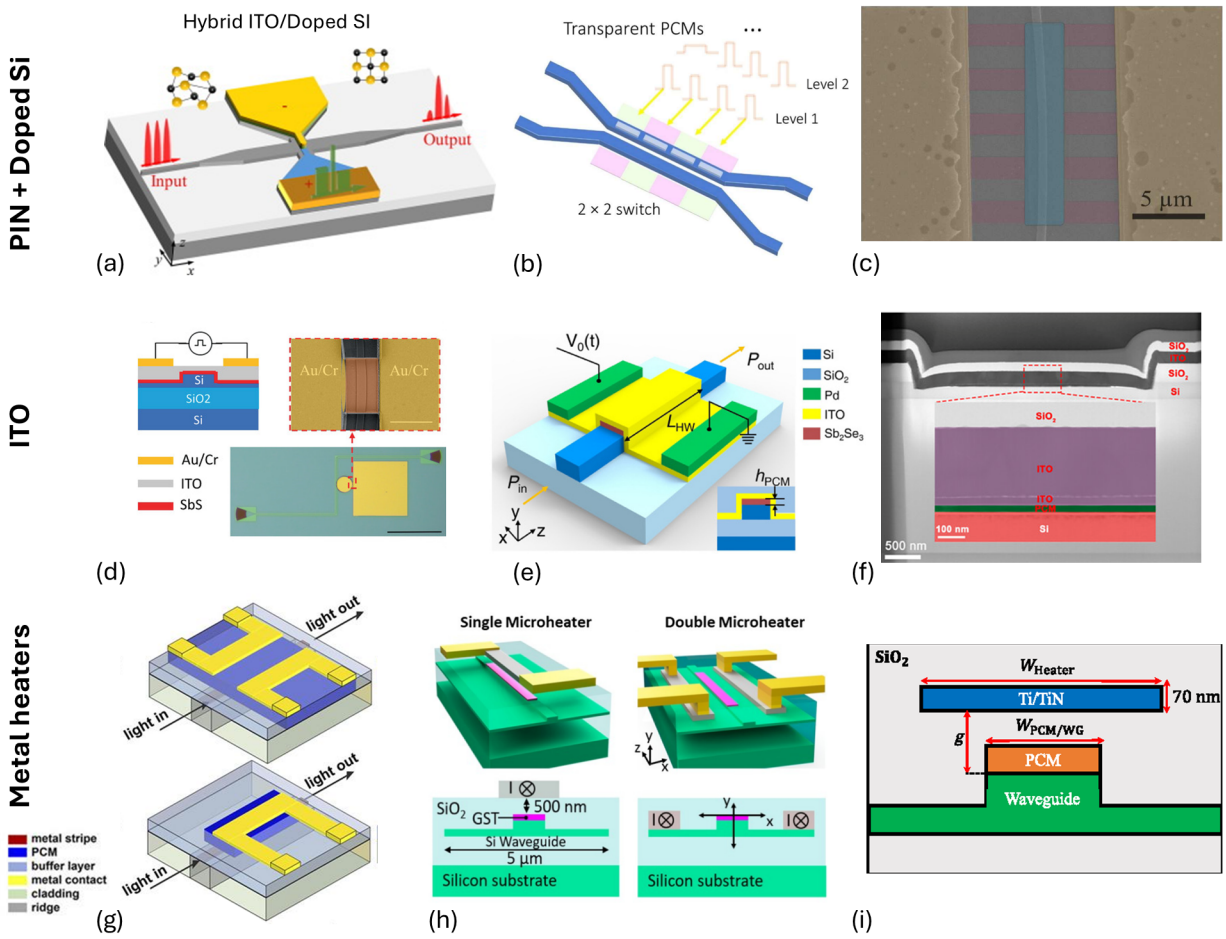

Figure 10: (a) Hybrid ITO-doped Si GST PIC device on a multi mode interferometer with current passing through the PCM [163]. (b) Alternating PIN junctions heater design with PCM on a directional coupler [179]. (c) Alternating doped-undoped regions in SOI waveguide with Sb_2Se_3 for controlled partial switching [180]. (d) Sb_2S_3 PIC design with continuous ITO and PCM layer. (Reprinted with permission from [181] ©John Wiley and Sons). (e) Schematic of Sb_2Se_3-based PIC with ITO heater for a Bragg reflector design. (Reprinted with permission from [182] ©Optica Publishing Group) (f) TEM of a cross-section through a Sn-GST-based PIC with recess in an SiO_2 cladding and ITO heater for improved reliability. (Reprinted with permission from [183] ©Optica Publishing Group). (g) Metal heater designs for a PCM-plasmonic type PIC [184]. (h) Metal heater designs for dielectric only PCM-based PIC (compared also against PIN junction heaters) (Reprinted with permission from [185] ©Optica Publishing Group). (i) Schematic of Ti/TiN metal heater for optimization of a PCM PIC design, including heater positioning [186].

demonstrated that incorporating a GSST/graphene microheater into the same logic circuit enables various fundamental logic operations (OR, NOR, AND, NAND) to be performed with low insertion loss (<1 dB), a high contrast ratio (>10 dB), and broadband operation (100 nm) within the telecommunications band.

3.3 Thermal transport considerations in PCM device integration

The unique set of properties displayed by PCMs (e.g., nonvolatility, large optical contrast, and reversible switching) has led to the development of optics-tailored materials and to their integration into an increasing number of devices for free-space and integrated photonics applications—the

emerging research areas of optical phase change materials [50, 187] and phase change photonics [188] are testaments of this. For most applications, from metasurfaces to PIC phase shifters and amplitude modulators, electro-thermal control of PCMs using microheaters has proved the optimal method to reversibly switch PCMs because *(i)* it allows switching arbitrarily large (>1 μm^2) areas, *(ii)* any PCM can be switched (as opposed to optical switching which works only if the material is absorptive), and *(iii)* it is a scalable process that allows the integration of many devices in both free-space and integrated approaches, as shown in Fig. 11. Optical switching mechanisms, whether using propagating modes within a waveguide [42, 189, 190] or free-space lasers [191, 192], are not scalable given the complexity of a reconfigurable device incorporating pump lasers. Moreover, since the strength of optical modulation depends on the volume of the material that is switched, the filamentation mechanism traditionally used in nanoelectronic crossbar devices does not suffice for most photonic applications. Hence, microheaters have been the best alternative; they offer an indirect Joule heating mechanism in which current does not flow through the PCM but rather remains within the higher electrically conductive material chosen for the heater. However, the PCM lies in direct contact; thus, thermal conduction dictates the temporal response of the heat stimuli. Microheaters can adopt arbitrary shapes and sizes; therefore, to optimize the performance of PCMs in functional devices, it is paramount to consider the intricate relationships between parameters such as the material and geometry of the microheater and the switching and thermal characteristics of the chosen PCM, as several groups have done [193, 180, 194].

The cooling rate is arguably the most critical characteristic of a microheater for PCM-based photonic devices. Since fast melt-quenching process is necessary for the amorphization of PCMs, the critical cooling rate must exceed a threshold value to prevent kinetically initiated crystallization [195]. Thus, choosing the right material for a microheater and engineering its thermal environment is critical, as discussed in Section 3. In addition to electrical conductivity, the thermal conductivity also needs to be high. The former allows enough power dissipation into Joule heating, and the latter allows fast heat dissipation once power is off, hence enabling melt-quenching. Considering materials with this combination of properties (see Table 3), metals are the first natural choice. However, the high optical losses introduced by metals mean that they can only be used in reflection-only free-space applications [50, 46]. Moreover, integrating metal microheaters into PICs has a complex thermal environment design, as the metal cannot be close to the waveguide and PCM, which compromises cooling rates [148]. To avoid this challenge, transparency has also been imposed as a top priority in the microheater's material properties list. Graphene has demonstrated the most energy-efficient approach in this direction, although it suffers from complex and low-yield fabrication [21, 19]. On the other hand, doped-silicon microheaters offer CMOS compatibility, high-yield fabrications, tailorable electrical conductivity, moderate thermal conductivity (see Fig. 11), and straightforward integration, since the same silicon used for the waveguides can be used as a microheater. Several approaches have taken advantage of these properties to demonstrate phase and amplitude modulators on integrated waveguides [45, 152, 165] and also large area devices for free-space metasurfaces with the added value of offering transparency in the near-infrared (see Fig. 11(b)). The only drawbacks of doped-silicon heaters are the trade-off between electrical conductivity and optical losses [45] and its large refractive index, which could introduce large perturbations to metasurfaces [19].

Regarding the geometry of the functional device, the first parameter we consider is the thickness of the PCM, which is restricted by its own crystallization kinetics [196]: the faster the crystallization, the thinner the films that can be reversibly switched. For instance, $Ge_2Sb_2Te_5$ can crystallize within a few tens of nanoseconds, leading to a critical cooling rate of the order of 10^9 °C/s and thus, a maximum thickness of around 150 nm [196], although no experimental result

with GST thicker than 80 nm has been demonstrated. On the other hand, slower alloys such as $Ge_2Sb_2Se_4Te$ with significantly slower crystallization kinetics [191] have enabled up to 180 nm-thick metasurfaces with over 13000 reversible cycles [164]. For integrated photonics, the modulation strength can be tuned by manipulating the PCM length along the waveguide with a thinner film. Thus, the maximum thickness is not critical. In contrast, since light propagates through the PCM, thickness becomes an important structural parameter when it comes to metasurfaces for free-space applications [149, 197, 46]. This requires careful design of the reflectance and transmittance responses.

Furthermore, while the area of the PCM (and/or heater) can, in principle, be arbitrary, the energy consumption and heating efficiency become limiting factors. Depending on the application, the switching area of the PCM could range from a few square micrometers in PICs to thousands in free space optics (see Fig.11 for comparison). However, it is important to consider that as the heater gets larger, the temperature uniformity needs to be carefully engineered to ensure that a large PCM film or pattern is uniformly switched [46]. In PICs, the switching area is highly dependent on the heater design, and this is critical since the spatial distribution of the amorphous and crystalline domains is the main mechanism behind the multi-level response required in most PCM-based analog photonic applications [187]. Although several groups have proposed waveguide-integrated microheaters, most of them can only achieve reliable binary switching between the fully amorphous and fully crystalline states, as in the case of graphene microheaters shown in Fig. 11(c) [21] and the doped-silicon heaters shown in Fig. 11(f) [45]. To achieve multilevel modulation, a precise area needs to be deterministically switched. This can be precisely controlled by tuning the energy of electrical pulses on a single heater with a well-designed thermal profile (see Figs. 11(g) and (h)) [198, 180]. Moreover, multiple heaters, each allowing bi-state switching, can also be used in series to partially control one PCM cell, as shown in Fig. 11(e) [199, 148]. In addition to controlling partial states, another important aspect is improving cyclability, as demonstrated by using a "trench-type" heater to reduce thermal stress in the cross section of the heater, as shown in Fig. 11(i) [183].

We now consider the switching speed of PCM-based photonic devices with microheaters. The first consequence of having large-area devices that require microheaters is the slower speeds compared to optical switching or direct electrical switching due to the larger thermal mass of the device and thus slower heat diffusion. However, a large area can be switched all at once in a task that can take longer if using scanning laser irradiation [31]. The time for a single switching event is the sum of the electrical pulse duration and the cooling time. The pulse width for PCM crystallization varies from tens of microseconds to hundreds of milliseconds and is dominated by the kinetic processes of nucleation and grain growth [202]. To minimize energy consumption, several doping techniques have been tested in PCMs to reduce their crystallization temperature [200, 183]. For amorphization, the pulse width ranges from hundreds of nanoseconds to a few microseconds and consumes several nanojoules to melt PCM, and, as explained above, this process must be followed by a fast quenching, which is determined by the thermal properties of the microheater and the device environment. It is important to note that there is a trade-off between heat dissipation (cooling rate) and power consumption, since high thermal conductivity enables faster cooling but also slows down the heating, thus requiring more power to reach melting temperature [203, 197, 19, 38]. Recent studies have shown that there is a minimum pulse width value to reach dynamic thermal equilibrium and maximize heat dissipation efficiency in doped silicon heaters with different geometries, which is important in device design [204]. Lastly, we consider the encapsulation of the PCM, which is critical in the integration of PCMs in active nanophotonic devices. Ranging from a few nanometers to hundreds of nanometers thick, the capping is an important parameter to be engineered since it plays multiple relevant roles but, at the same time, can af-

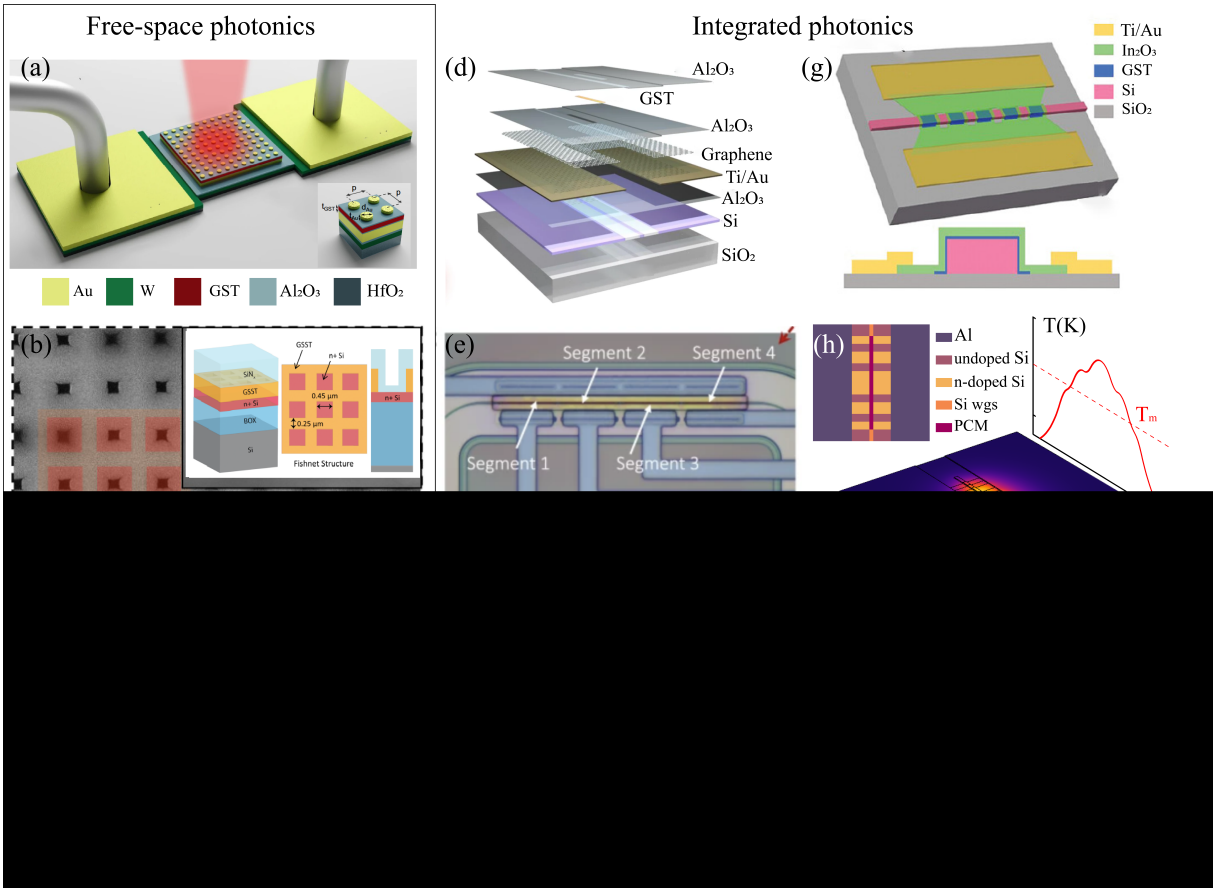

Figure 11: Nanophotonic devices with active reconfiguration using PCMs and integrated microheaters. (a) Schematic of a tungsten heater for GST-based metasurfaces [149]. (b) Schematic of n-doped silicon heater on a transmissive filter in the C-band [35]. (c) Optical and thermal image of FTO-based smart glazing pixel on silica [200]. (d) Schematic of graphene heater for integrated photonics [21]. (e) Optical image of multi-bi-state-switching PIN heater device for multilevel switching [201]. (f) SEM image of n-doped bowtie heater [45]. (g) Schematic of In_2O_3 heater with waveguides for multilevel switching [198]. (h) Schematic of multi-width bridge for multilevel switching [180]. (i) Schematic of "Trench" ITO heater[183]

fect the thermal properties. For instance, a capping layer–often oxides such as SiO_2 or Al_2O_3, nitrates like Si_3N_4, or composite dielectrics like ZnS-SiO_2–serves to protect the PCM from oxidation and introduces strain to help prevent delamination and other failure mechanisms [164, 205, 206]. However, it can also decrease the thermal conductivity of the device if convection and conductivity to an air cladding are prevented.

4 Phase change materials selection

In this section, we review some of the recent and novel PCMs which are relevant to photonic applications and consolidate them in a table for the PCMs [174, 210, 211, 212, 213, 150, 214, 215, 51, 216] along with the most recent advancements including superlattice and halide materials [217, 218, 219]. When it comes to material selection, we can think about what the ideal PCM would be for a given device application, with a focus on practical considerations such as the length scale limitation, large optical contrast, phase stability, fast switching, high thermal conductivity, low melting point, simple stoichiometry, small volume change upon phase transition, and more. Key

Table 3: Functional PCM devices featuring electro-thermal switching with optical readout in Fig. 11 and electrical readout

Optical readout

PCM	Heater	Thickness nm	Speed Hz	Area/length $\mu m^2/\mu m$	Energy per switch(amor./cry) μJ	reference
$Ge_2Sb_2Te_5$	W	40	5k	80×80	0.06/11.56	[149]
$Ge_2Sb_2Se_4Te$	N-doped Si	220	5	140×140	$480/7.7\times10^6$	[35]
Sn-doped $Ge_{20}Te_{80}$	FTO	12	5k	50×50	22/44	[200]
$Ge_2Sb_2Te_5$	Graphene	23	8k	4.73	$5.55\times10^{-3}/0.86$	[21]
Sb_2S_3	PIN Si diode	20	5	80	$3.37/2.25\times10^3$	[199]
Sb_2Se_3	N-doped Si	30	1k	6	0.046/10.24	[45]
$Ge_2Sb_2Te_5$	**In_2O_3**	15	10k	18	0.12-0.45/0.25-9	[198]
$Ge_2Sb_2Se_4Te$	N-doped Si	30	100	12	0.65-1.27/440	[180]
Sn-doped $Ge_2Sb_2Te_5$	**ITO**	20	20k	3	0.2/0.75	[183]

Electrical readout

PCM	Heater	Thickness nm	Speed Hz	Cross-section area μm^2	Switching voltage(amor./cry) V	reference
$Ge_2Sb_2Te_5$	W	50	10M	0.28×0.035	10/5	[207]
$Ge_{0.55}Sb_{0.9}Te_{1.9}$	Pt	500	500k	0.5×0.5	5.5/5	[208]
$Ag_5In_5Sb_{60}Te_{30}$	Ti	80	10M	Not provided	1.6/0.3	[209]

advances in material research are essential for establishing manufacturing scalability and reliability to transition from laboratory to commercial use, even for niche applications [220, 196, 4].

For this survey, Ge-Sb-Te (with alloys such as $GeSb_4Te_7$ and $Ge_2Sb_2Te_5$) was selected as the starting material. The Ge-Sb-Te alloys are identified along a pseudo-binary line that connects the GeTe and Sb_2Te_3 compounds. In general, moving from GeTe towards Sb_2Te_3 on the pseudo-binary line, the compound demonstrates a higher nucleation rate with smaller stochasticity, resulting in an increase in crystallization speed, glass-transition temperature (T_g), melting temperature (T_m), and data retention (i.e., the stability of the amorphous state) decrease[221, 222, 223]. In other words, Sb_2Te_3 offers the lowest crystallization temperature (∼423 K), but its amorphous state is unstable [212]. In contrast, GeTe offers a very stable amorphous phase, but at the cost of a slightly higher crystallization (∼473 K) and melting (998 K) temperature. Films with stoichiometric composition, Te and GeTe, can be crystallized using laser pulses of less than 100 ns duration[224]. Therefore, a compromise between the crystallization speed and the amorphous stability can be made by selecting a ternary composition close to the center of the pseudo-binary line. Standing out in the pool of Ge-Sb-Te, $Ge_2Sb_2Te_5$ (GST) offers a large optical contrast emanating from the pronounced change of local atomic arrangement and fast crystallization speed (< 100 ns) with moderate T_g (100 – 150°C) that ensures long-term data retention (∼10 years)[225, 226]. Additionally, GST is reported to be tolerant to ionizing radiation effects due to the appreciable void volume present in the amorphous state arising from collisions inside the glass structure[227]. The diversity of bonding environments present in the PCM likely lowers the energy barrier for structural reconfiguration, thereby accelerating the bond reformation and thus facilitating the recovery process of the amorphous network after irradiation[227, 228]. Key advances have also been made in GST survivability qualification in the space environment through the Materials International Space Station Experiment-14 (MISSE-14) mission in the International Space Station (ISS)[7]. These characteristics make PCMs an attractive materials platform for spaceborne photonics applications, promising robust, lightweight, and energy-efficient reconfigurable opti-

cal systems whose functions can be dynamically defined on-demand and in orbit to deliver enhanced science or mission support in harsh environments[229]. However, GST is limited by low thermal stability and a ∼7% volumetric expansion following the crystalline-to-amorphous conversion [230, 107].

PCMs such as Sb_2Se_3, Sb_2S_3, GaS, GeTe have also been studied [210, 212, 51, 231]. A refractive index contrast of Δn =0.60 at 1550 nm wavelength for Sb_2S_3 and Δn =0.77 at 1550 nm for Sb_2Se_3 are reported, while maintaining low losses at near-IR telecommunication wavelengths, making these materials well matched to the silicon photonics platform [212]. Moreover, the thermal conductivities of Sb_2S_3 and Sb_2Se_3 increase by a factor of 2 (to 0.66 and 0.72 $Wm^{-1}K^{-1}$ respectively) upon being cooled to room temperature after heating to 320°C[51]. GaS also shows low-loss, k=0, with high index contrast of Δn =0.50 at the C-band as well as between amorphous and crystalline phase transitions by picosecond green laser irradiation[210]. These results open a new direction in programmable integrated photonic circuits, switchable metasurfaces, and reconfigurable nanophotonic devices including telecommunication. Controlling the optical properties of binary GeTe demonstrates the specially tunable and low-emissivity coating, which modulates the solar heat gain of a window while maintaining neutral coloration and constant transmission of light at visible wavelength – an impossibility for materials with fixed thermal and optical properties[200]. The melting temperature and crystallization kinetics can be tuned by controlling the atomic ratio of Ge and Te [224]. It has been shown that varying the Ge content from ∼30% to ∼70% changed the crystallization time by 3 orders of magnitude for 50 nm GeTe films deposited on 1µm SiO_2[232]. Doping with Sn further lowers the GeTe amorphization melting temperature from 700 K to 557 K during the structural transition from rhombohedral (R) to cubic (C), with comparable optical properties of undoped GeTe [233]. Such an R-C structural conversion is revealed with increasing Sn content; ∼3.0% Sn preserves the GeTe rhombohedral (R) structure, whereas a Sn content of ∼25.0% exhibits a cubic (C) structure. Compared with undoped GeTe, Sn displays a ∼3.0% increase in crystalline resistance and a resistance ratio (high/low) of 10^5 [234], satisfying the requirements of lower programming currents for memory application. This is similar to Sn-doped GST: the melting points of $Sn_{9.8}Ge_{20.3}Sb_{28.4}Te_{41.5}$ and $Sn_{18.8}Ge_{19.5}Sb_{25.3}Te_{36.4}$ are 748 K and 723 K, respectively, much lower than GST 913 K [235].

The transformation to liquid phase during the amorphization cycle can accelerate various device failure mechanisms such as segregation, de-wetting, void formation, and delamination. To address this, a layered binary PCM, In_2Se_3, which displays phase-change behavior at the interface of adjoining layers, was developed to have a melt-free β-to-γ phase change that is expected to result in longer device lifetimes [174]. Contrary to typical PCMs, both the β and γ states of In_2Se_3 are crystalline; they are crystal polymorphs with slightly different configurational entropies resulting from different bond geometries (octahedral vs tetrahedral) and stacking schemes (rhombohedral vs hexagonal). This contrast in configurational entropy is sufficient to stabilize both phases over distinct temperature ranges, allowing for the desired SET/RESET behavior in electronics and photonics applications. The single element of antimony (Sb) has been demonstrated in phase change memory applications as an example of a simple, monatomic PCM [216]. It was shown that amorphous Sb is a semiconductor while crystalline Sb is a metal, yielding the desired contrast in electrical resistivity [236]. This compositional simplification and the naturally most homogenous of Sb improve reliability without phase segregation and eliminate problems related to unwanted deviations from the optimized stoichiometry in the switching volume, which become increasingly pressing when devices are aggressively miniaturized for niche applications.

PCMs can also substantially impact metasurface-based optics applications, provided that material improvements and manufacturing batch size continue to scale upwards. One strategy to

achieve this relies on mixing precise amounts of different atoms, often resulting in quaternary or even more complicated compounds – for example: Ag- and In-doped Sb_2Te alloy (Ag-In-Sb-Te, AIST), $Ge_2Sb_2Se_2Te_1$, $Ge_{20}Sb_{20}Se_{20}S_{20}Te_{20}$, $NaIn_3Se_5$, as well as other quaternary and quinary PCMs, to tailor optical characteristics and improve switching cycling performance [211, 150, 214, 215, 237]. In the case of AIST, indium doping accelerates the crystallization and hence operation speed while Ag doping limits the random diffusion of In atoms and enhances thermal stability of the amorphous phase[215]. Another quaternary PCM is GSST. The substitution of Te in GST alloys with selenium (Se) atoms forms Ge-Sb-Se-Te that is referred to as GSST [219, 238]. The stoichiometry $Ge_2Sb_2Se_4Te$ shows broadband transparency in the near- to mid-IR spectral range while offering a large refractive index change ($\Delta n \approx 1.5$) with minimal loss penalty (i.e., $\Delta k \approx 0$) which claims figure-of-merit (FOM = Δn /Δk) over two orders of magnitude larger than that of GST alloys. Increasing the Se content in GSST monotonically increases the crystallization temperature, which translates into a better stability of the amorphous phase. However, this stability comes at a major drawback of slow crystallization speed as Se replaced the Te in a GST alloy. The total time for crystallization completion of GSST is ∼10 ms compared to ∼100 ns of GST[150]. In integrated photonics, the GSST-formed devices outperformed due to large switching contrast and low insertion loss, but due to the large optical losses in the visible spectrum, GSST is still non-ideal for photonic devices such as holographic displays, color filters, etc[239, 240]. As a follow-up to the recent discovery of GSST and trends on bringing distinguished functionality of each chalcogen type (S, Se, or Te) into compounds, Sb-rich equichalcogenides (containing S, Se, and Te in equal proportions) such as $Ge_{15}Sb_{40}S_{15}Se_{15}Te_{15}$, $Ge_{20}Sb_{20}S_{20}Se_{20}Te_{20}$, quinary PCM, have been reported[214]. The driving factors for adding Ge is to improve the amorphous phase stability; adding Se into the composition is for the improved glass forming ability; S can further suppress optical losses; Te is to introduce resonant bonding and boost index contrast [241]. Equichalcogenide GeSbSeSTe bulk glass from thermal stability and optical properties shows promise for applications in photonics and metasurface optics[214].

Heterostructure PCM. A major source of power consumption in PCMs is the energy required to reorient the atoms into different structural motifs. More than a decade ago, researchers have shown that by restricting the movement of atoms to a single direction, the entropic losses associated with the phase change process can be substantially mitigated. In this respect, R. E. Simpson et al.[217] reported an order of magnitude reduction in power consumption in the set process using a superlattice of crystalline $GeTe/Sb_2Te_3$ bilayers compared to bulk $Ge_2Sb_2Te_5$ alloy. These weakly coupled heterostructures exhibit novel behavior distinct from conventional 2D and 3D materials, as they have smaller interlayer spacing than typical van der Waals interactions while lacking covalent bonding [242]. The switching mechanism in superlattice structures is often attributed to interface effects and changes in bonding characteristics driven by Ge atom motion, rather than a conventional amorphous-to-crystalline phase transformation [218]. However, some studies suggest that the switching behavior stems from a thermal melt-quench process rather than purely electronic transitions [243]. Recent experimental findings have further challenged the Ge atom motion hypothesis in superlattice PCMs. Observations of intermixing between GeTe and Sb2Te3 layers at the interface cast doubt on the role of Ge motion in the switching process [244]. Supporting this, molecular dynamics simulations reveal partial melting and suggest that the switching mechanism in $GeTe/Sb_2Te_3$ superlattices results from distinct nucleation and crystallization behaviors compared to GST alloy. These simulations suggest a melting mechanism distinct from that of GST alloys, characterized by a more localized and controlled process. This partial melting results in a post-melt atomic structure that is more chemically ordered than that of conventional GST alloys [245].

Regardless of the underlying switching mechanism, these superlattices have demonstrated high-

endurance performance with minimal drift in their electrical properties upon cycling for memory applications [135]. The lower thermal load requirement in PCM heterostructures also lends itself to a faster switching speed (since less heat needs to be accumulated and dissipated) as well as improved thermal stability (since the temperature gradients need not be as large to achieve tuning). Notably, the failure time of the superlattice was found to outperform that of GST at a given temperature [246]. However, despite the lower switching energy (three orders of magnitude reduced compared to bulk alloys) and recent progress in materials physics, these interface-based superlattice PCMs have not been well studied for photonics applications, largely due to the lack of published optical constants required for device design and optimization [247].

Beyond these approaches, recently, perovskite halide materials, (BA_2PbI_4) have been studied for identifying the phase-transition and refractive index change around room temperature[238] and for visible wavelength applications. With this novel approach of halide perovskites, we expand the relatively limited PCMs library for realization of active metasurface optics in the visible spectrum for applications in light-emitting devices, displays and spatial-light-modulators[238]. Additionally, there have been several recent studies on transition-metal-based structural PCMs, MoS_2, TiS_2, ZrS_2, $MoTe_2$, WTe_2, and Cu_2GeTe_3, all of which are layered transition metal dichalcogenide (TMD) van der Waals (vdW) materials. [248, 249, 250, 251]. Weak vdW bonds between layers suggest process compatibility and easy integration with various material platforms as candidates for phase change photonic materials [249, 250, 251]. Phase-change functionality (i.e., transformation between layered polymorphs) at room temperature has been demonstrated for tellurides including $MoTe_2$ and (Mo, W)Te_2 [249]. $MoTe_2$ is a semiconductor in the 2H structure in its ground state and can be prepared as a semi-metal in the 1T' structure as a metastable state. WTe_2 is a semi-metal in the Td structure in its ground state and could be a semiconductor in the 2H structure as a metastable state. This diffusionless, order-order transformation, the martensitic phase transformation between 2H and 1T structures, is expected to be faster, require less energy, and to cause less fatigue than melt-quench and recrystallization transformations needed for GST [249, 250, 251]. Moreover, several non-stoichiometric polymorphs of $MoTe_2$ have strong optical contrast, ($\Delta n \sim 1$) between phases,comparable to established PCMs like GST and GSST, in the NIR with low loss [249].

Lastly, it was very recently shown that high-throughput computational screening based on density functional theory-based molecular dynamics and machine learning can successfully discover new phase-change alloys based on similar vdW-like material motifs [252]. The novel discovery framework claims to have successfully identified 25 new 2D chalcogenide alloys based on the $CrGeTe_3$ structural prototype; three of the predicted materials - $CrSiTe_3$, $InGeTe_3$, and $AlSiTe_3$ - were grown and characterized successfully as examples to validate the computational approach. The compounds showed crystallization temperatures of 623 K, 533 K, and 723 K, respectively. Though switching speeds have not yet been characterized, they are expected to be relatively fast due to the layered nature of the materials, although the relatively high crystallization temperatures may cause a slower switching speed than the previously discussed In_2Se_3 or superlattice structures. A summary of recent materials development in PCMs is shown in Table 3.

Table 4: Room temperature thermal properties of PCMs in amorphous and crystalline states. Unmeasured properties are left blank.

PCM	Phase	T_{crys} K	T_{melt} K	Specific Heat J kg^{-1} K^{-1}	Density kg m^{-3}	Thermal conductivity W m^{-1} K^{-1}	Crys. Speed ns
$Ge_2Sb_2Te_5$	am.	415[253]	889[253]	221[254, 107]	5870[225]	0.20	$<10^2$[255]
	crys.	-	-	223[254, 107]	6270[225]	1.02	-
$Ge_2Sb_2Se_4Te$	amor.	550[19]	890[19]	285[49]	5270[19]	0.20[49]	$\sim10^7$[191]
	crys.	-	-	325[49]	5530[49]	0.48[49]	-
GeTe	amor.	443[256]	998[257]	-	5610[258]	0.20[259]	$\sim10^2$[224]
	crys.	-	-	256[260]	5910-6180[259, 261]	3.2-3.6[262, 259]	-
Sb_2Se_3	amor.	473[212]	885[263]	-	-	0.22	$\sim10^7$[212]
	crys.	-	-	263[264]	5840[265]	0.72	-
Sb_2S_3	amor.	543[212]	823[266]	-	4150[267]	0.21	$\sim10^8$[212]
	crys.	-	-	368[268, 269]	4640[267]	0.74	-
$InSe_3$	β	473[174]	-	-	5670[270]	0.32[271]	$\sim10^1$ [174]
	γ	623[174]	-	-	5750 [272]	0.35[272]	$\sim10^2$ [174]
GaS	amor.	623-723 [210]	-	-	-	0.7$\parallel$, 10$\perp$[273]	-
	crys.	-	-	-	-	-	-
Sb	amor.	468[216]	-	$\sim$2100	6690	-	$\sim10^1$[216]
	crys.	-	903	-	6690	24.4	$\sim10^2$[216]
$Ge_{10}As_{22}Se_{68}$	amor.	438[211]	603[274]	-	4600[274]	0.2[274]	-
	crys.	-	-	-	-	-	-
Ge-Sb-Se-S-Te	amor.	423[214]	-	-	-	-	-
	crys.	-	-	-	-	-	-
AIST	amor.	423[211]	817[211]	-	6420[275]	-	-
	crys.	-	-	-	-	-	-
$Sc_xSb_2Se_3$ (0.1<x<0.3)	amor.	$\sim$411[276]	-	-	-	-	$\sim10^0$[276]
	crys.	-	-	-	-	-	-
$GeTe/Sb_2Te_3$ superlattice	high-ρ	$\sim$423-498[218]	-	-	-	$\sim$0.5[277]	$\sim10^0$[218]
	low-ρ	-	-	-	-	-	$\sim10^2$[218]
BA_2PbI_4	amor.	513[238]	-	-	-	-	-
	crys.	-	-	-	-	-	-
CrGT prototypes	high-ρ	533 - 723[252]	-	-	-	-	-
	low-ρ	-	-	-	-	-	-

PCM To optimize the performance of PCMs in functional device, not only the right material for the microheater, but also the choice of PCM is crucial. However, PCM requirements in both electronic and photonic applications are vast and very application-dependent [220]. While electrical PCMs typically rely on high switching speeds (∼ns) and a large contrast in resistance states (ON/OFF) [278, 149], photonic applications span a broader range of speed requirements, from sub-nanosecond to milliseconds, and may benefit from either lossy or lossless states in the PCM. For instance, some photonic filters might require a lossy crystalline state, whereas photonic phase shifters demand both lossless amorphous and crystalline states [279]. Given the wide variety of application-specific requirements, it is crucial to evaluate the properties of different PCMs and their suitability for a specific application when selecting a material [4].

While some parameters are specific to particular applications, others are almost ubiquitously relevant. One critical factor is the crystallization speed of glasses and amorphous materials, which directly affects the data rate and set power in electronic memory devices. The crystallization speed of the PCMs either increases or decreases at reduced dimensions, depending on the material composition [280, 281]. Another key parameter is the reduced glass temperature, $T_{rg} = T_g/T_m$, which represents the ratio of the glass transition temperature T_m over glass melting temperature T_m. Typically, T_g is expected to be high and T_m is expected to be lower on reset power and a lower melting temperature is generally favorable, implying that less power would be needed in the power limiting reset step in functional devices. T_{rg} is always less than 1 but a higher T_{rg} often indicates better glass-forming ability because it suggests that the material is more likely to bypass crystallization during cooling and form an amorphous structure [281, 282]. The crystal nucleation rate and crystal growth velocity crucially depend on the glass transition temperature and systematic trends for the crystallization kinetics in PCMs, along the GeTe-GeSe, GeTe-SnTe, and GeTe-Sb_2Te_3 pseudo-binary lines were reported [283, 223]. These developments reveal that the nucleation rate governs both the crystallization speed as well as the origin of the stochasticity of crystallization for PCMs. Upon systematic changes in stoichiometry, the speed of crystallization changes by three orders of magnitude concomitantly with pronounced changes in stochasticity - $Ge_2Sb_2Te_5$ and $Ge_3Sn_2Te_5$ identify as fast-nucleation materials while GeTe, AIST, and Ge_2SeTe are slow-nucleation materials [223]. Again, the PCMs requirements for the functional device especially, photonics is extremely application-specific but the systematic trends for the crystallization kinetics is a quantum-chemical map and provides a blueprint to design crystallization kinetics and database for the right choice of the PCMs of the crucial crystallization speed and glass transition temperatures.

As new materials develop, consolidated PCM databases with diverse categories such as band gap (for wavelength specified transmittance), melting temperature (for energy consumption estimation), scalability, optical contrast and loss, and heat uniformity will prove invaluable for finding PCMs for a given application, potentially in a "plug-and-play" style [284]. Looking at PCMs from these practical standpoints may also help generate more demanding test platforms for evaluating materials for specific applications.

5 Modeling thermal transport characteristics

Improving the performance and reliability of PCM-based devices necessitates an accurate understanding of the temperature distribution within the PCM and the resulting thermal stress on adjacent materials. This becomes even more critical as the PCM volume increases beyond several tens of microns, leading to a more pronounced temperature gradient and subsequent non-

uniformity upon phase transformation [205]. Experimentally measuring the temperature distribution during phase transformation presents significant challenges, necessitating exceptionally precise setups with high spatial and temporal resolution [285]. In this respect, computational techniques could substantially help in providing a better understanding of the phase transformation dynamics as well as an estimate for the temperature gradient within the device at various stages of the phase transformation [91].

Thus far, due to widespread application of chalcogenides in sub-micron memory devices, which are less sensitive to temperature gradients, a vast majority of research has been focused on atomistic simulations such as density functional theory (DFT) and ab-initio molecular dynamics (AIMD) to understand the nucleation and growth processes [286, 287, 288, 289], bonding properties [228, 64, 290], and carrier dynamics [95, 71]. However, as PCMs find application beyond storage-class technologies with larger active volumes, there is a growing demand for a better understanding of material performance within device ensembles at larger length scales, involving systems beyond thousands of atoms and nanoseconds in duration. Consequently, there has been a rising interest in modeling PCM behavior at larger length scales, particularly in photonic systems [193, 291, 19, 148]. This is partly achieved through recent advancements in machine learning algorithms, which combine the efficiency of empirical potentials with the accuracy of DFT [292, 293], as well as finite element (FE) models to enhance the operational efficiency of the overall device [91]. In the following, we will briefly review some of the recent advancements in FE modeling that are most relevant to the content discussed.

A crucial aspect of FE simulations in PCM-based devices is the accurate representation of thermophysical properties, including thermal conductivity, interfacial thermal resistance, coefficient of thermal expansion, heat capacity, switching temperature, enthalpy of fusion, and density. The sensitivity of simulation results to these parameters can vary depending on the material, device size, and architecture. For instance, in crystalline GST, the Kapitza length at tungsten interfaces can reach up to 25 nm[107]. Consequently, in the simulation of memory cells[294], where the PCM size is on the order of tens of nanometers—comparable to the Kapitza length—interfacial thermal resistance significantly impacts the temperature distribution and must be included in the model[62, 107]. However, in systems like metafilters[35], where the PCM size is much larger than the Kapitza length, interfacial thermal resistance has a negligible effect on thermal transport.

Beyond temperature distribution, FE simulations can offer valuable insights into other critical factors affecting device performance, such as thermal stress[297], cooling rate[298], thermoelectric effects[299], stochasticity of nucleation and growth[300, 301, 302], and importantly, power consumption[303, 304]. FE simulations provide a reliable platform for designing and optimizing PCM-based devices before experimental fabrication. For example, Zheng et al.[193] used FE simulations to assess power consumption by comparing different heaters for switching 20 nm of GST integrated into a nanophotonic circuit, showing that switching could be achieved in as little as 12.5 ns with pulse energy as low as 6.6 aJ nm^{-3}. Figure 12 illustrates the temperature response comparison for graphene, ITO, and doped silicon heaters. These simulations revealed that graphene's ultra-low heat capacity and high in-plane thermal conductivity result in faster switching speeds and lower power consumption. This was later validated experimentally with GST on a single-layer graphene microheater in a waveguide configuration, achieving a switching energy density of 8.7 aJ nm^{-3} [21], demonstrating strong agreement between simulation and experimental results. Zhuo et al.[295] further showed that sandwiching a graphene heater between two PCM layers allows modulation of thicker PCMs, up to 280 nm. Figure 12(b) shows a schematic of the device configuration with the temperature gradient across the heater and temperature excursion during amorphization cycle. As discussed in earlier sections, temperature nonuniformity is a major cause

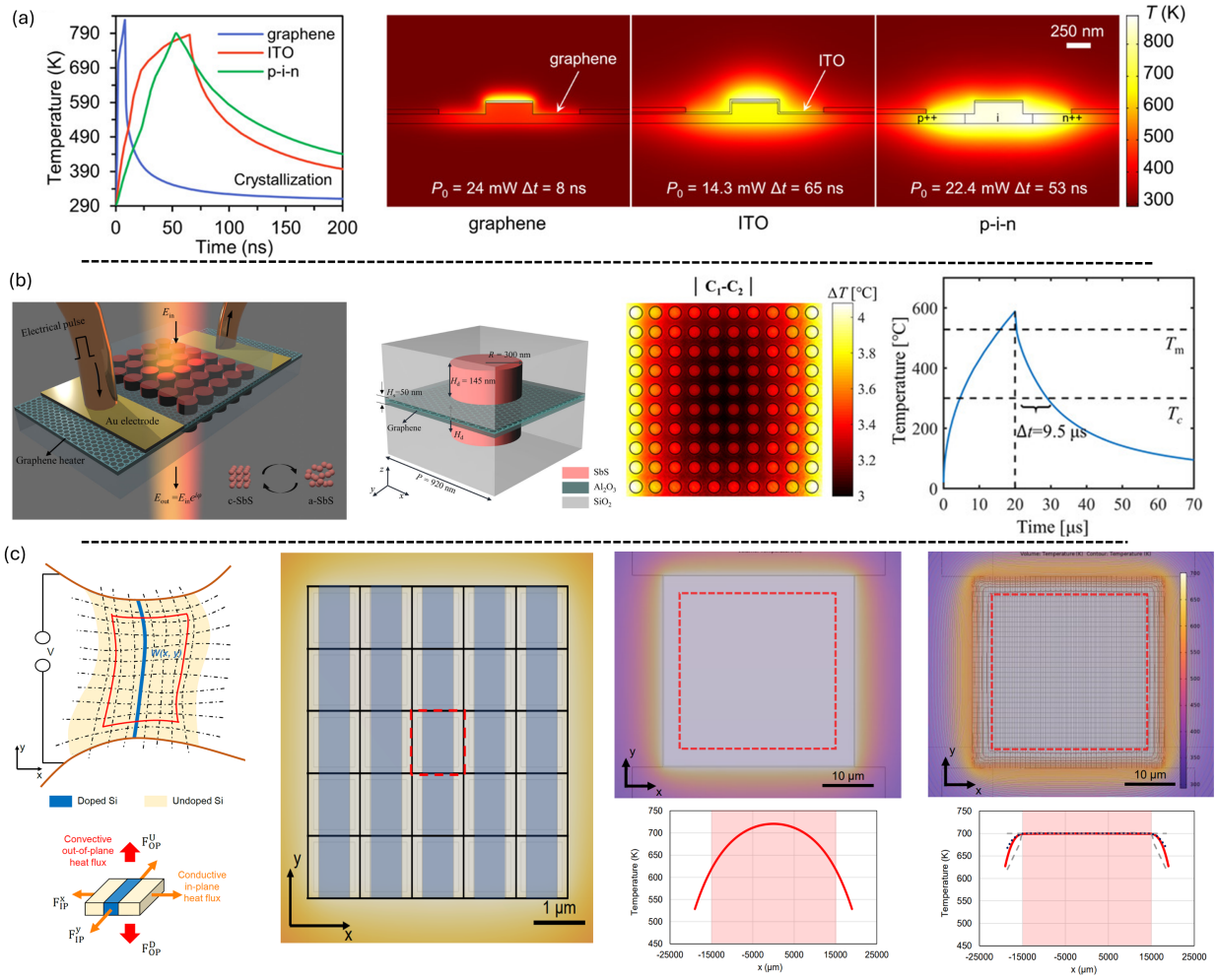

Figure 12: (a) Temperature profile and corresponding 2D temperature distribution during crystalline to amorphous phase transformation for various heater materials. Adopted with permission [193]. © 2020 American Chemical Society. (b) Schematic of the proposed sandwiched configuration to enhance phase transformation across the thickness of the PCM. Adopted with permission [295]. © 2022 Wiley-VCH GmbH. (c) Proposed microheater discretization approach to achieve a more uniform temperature distribution by controlling doping concentration in each section of the doped silicon microheater. Adopted with permission [296]. © 2024 AIP Publishing.

of device failure. To address this, an inverse design scheme has been proposed that can implement on-demand temperature profiles by varying the shape of doping regions in a binary doped Si microheater[296]. Figure 12(c) compares the temperature profile of a uniformly doped versus an inverse designed microheater. In the traditional uniformly doped design, the temperature gradient can reach up to 100 K from the center to the edges, whereas the latter results in a uniform temperature distribution with less than 0.2 K variation. This study offers a highly effective approach for achieving temperature uniformity across the heater.

6 Summary

Phase change materials have proven highly effective as the core technology in storage-class devices, such as rewritable optical discs and phase change memory, withstanding over 10^9 cycles. In recent years, they have become increasingly popular in reconfigurable photonics due to their

large change in refractive index upon phase transformation. However, the length scale required for photonic applications is orders of magnitude larger than that used in storage-class devices. This dramatic increase in switching volume introduces several thermal challenges that can lead to premature device failure and significantly reduced durability. Addressing these thermal considerations is crucial, and we explored this issue in depth, from the underlying physics to device integration. This review leverages recent studies to offer a unified understanding of thermal transport processes in PCM devices, aiming to extend the effective switching area beyond several tens of microns. It covers the thermal properties of key PCMs, along with an analysis of the microheaters used to switch the PCM and their power consumption. We also surveyed the literature to gather thermal properties of the most widely used PCMs, particularly for photonic applications, and consolidated these key properties into a table to aid in materials selection and modeling. This review brings together all the essential parameters for designing PCM-based devices for photonic applications and highlights the challenges that must be addressed before device fabrication. We hope this paper serves as a valuable reference for the development of future PCM-based devices at larger length scales, paving the way for more efficient and scalable technologies.

Acknowledgements

We appreciate support from Air Force Office of Scientific Research Grant No. FA9550-22-1-0456 and National Science Foundation Award No. 2225968.

References

[1] S. Abdollahramezani, O. Hemmatyar, H. Taghinejad, A. Krasnok, Y. Kiarashinejad, M. Zandehshahvar, A. Alù, A. Adibi, *Nanophotonics* **2020**, *9*, 5 1189.

[2] K. J. Miller, R. F. Haglund, S. M. Weiss, *Optical Materials Express* **2018**, *8*, 8 2415.

[3] C. Xiang, S. M. Bowers, A. Bjorlin, R. Blum, J. E. Bowers, *Applied Physics Letters* **2021**, *118*, 22.

[4] T. Gu, H. J. Kim, C. Rivero-Baleine, J. Hu, *Nature Photonics* **2023**, *17*, 1 48.

[5] W. Bogaerts, D. Pérez, J. Capmany, D. A. Miller, J. Poon, D. Englund, F. Morichetti, A. Melloni, *Nature* **2020**, *586*, 7828 207.

[6] P. Pitchappa, A. Kumar, S. Prakash, H. Jani, T. Venkatesan, R. Singh, *Advanced Materials* **2019**, *31*, 12 1808157.

[7] H. J. Kim, M. Julian, C. Williams, D. Bombara, J. Hu, T. Gu, K. Aryana, G. Sauti, W. Humphreys, *npj Microgravity* **2024**, *10*, 1 20.

[8] M. Wuttig, H. Bhaskaran, T. Taubner, *Nature photonics* **2017**, *11*, 8 465.

[9] W. Zhang, R. Mazzarello, M. Wuttig, E. Ma, *Nature Reviews Materials* **2019**, *4*, 3 150.

[10] A. Krasnok, M. Caldarola, N. Bonod, A. Alú, *Advanced optical materials* **2018**, *6*, 5 1701094.

[11] A. Tittl, A. John-Herpin, A. Leitis, E. R. Arvelo, H. Altug, *Angewandte Chemie International Edition* **2019**, *58*, 42 14810.

[12] Y. Qu, Q. Li, L. Cai, M. Pan, P. Ghosh, K. Du, M. Qiu, *Light: Science & Applications* **2018**, *7*, 1 1.

[13] M. N. Julian, C. Williams, S. Borg, S. Bartram, H. J. Kim, *Optica* **2020**, *7*, 7 746.

[14] S. Gyger, J. Zichi, L. Schweickert, A. W. Elshaari, S. Steinhauer, S. F. Covre da Silva, A. Rastelli, V. Zwiller, K. D. Jöns, C. Errando-Herranz, *Nature communications* **2021**, *12*, 1 1408.

[15] M. R. Watts, J. Sun, C. DeRose, D. C. Trotter, R. W. Young, G. N. Nielson, *Optics letters* **2013**, *38*, 5 733.

[16] D. J. Thomson, F. Y. Gardes, J.-M. Fedeli, S. Zlatanovic, Y. Hu, B. P. P. Kuo, E. Myslivets, N. Alic, S. Radic, G. Z. Mashanovich, et al., *IEEE Photonics Technology Letters* **2011**, *24*, 4 234.

[17] Z. Zhang, Z. You, D. Chu, *Light: Science & Applications* **2014**, *3*, 10 e213.

[18] C. Ríos, N. Youngblood, Z. Cheng, M. Le Gallo, W. H. Pernice, C. D. Wright, A. Sebastian, H. Bhaskaran, *Science advances* **2019**, *5*, 2 eaau5759.

[19] C. Ríos, Y. Zhang, M. Y. Shalaginov, S. Deckoff-Jones, H. Wang, S. An, H. Zhang, M. Kang, K. A. Richardson, C. Roberts, et al., *Advanced Photonics Research* **2021**, *2*, 1 2000034.

[20] M. Delaney, I. Zeimpekis, H. Du, X. Yan, M. Banakar, D. J. Thomson, D. W. Hewak, O. L. Muskens, *Science Advances* **2021**, *7*, 25 eabg3500.

[21] Z. Fang, R. Chen, J. Zheng, A. I. Khan, K. M. Neilson, S. J. Geiger, D. M. Callahan, M. G. Moebius, A. Saxena, M. E. Chen, et al., *Nature nanotechnology* **2022**, *17*, 8 842.

[22] W. Kim, M. BrightSky, T. Masuda, N. Sosa, S. Kim, R. Bruce, F. Carta, G. Fraczak, H.-Y. Cheng, A. Ray, et al., In *2016 IEEE International Electron Devices Meeting (IEDM)*. IEEE, **2016** 4–2.

[23] C. D. Wright, Y. Liu, K. I. Kohary, M. M. Aziz, R. J. Hicken, *Advanced Materials* **2011**, *23*, 30 3408.

[24] D. Ielmini, H.-S. P. Wong, *Nature Electronics* **2018**, *1*, 6 333.

[25] J. Feldmann, N. Youngblood, C. D. Wright, H. Bhaskaran, W. Pernice, *Nature* **2019**, *569*, 7755 208.

[26] A. Sebastian, M. Le Gallo, E. Eleftheriou, *Journal of Physics D: Applied Physics* **2019**, *52*, 44 443002.

[27] Q. Xia, J. J. Yang, *Nature materials* **2019**, *18*, 4 309.

[28] A. Sebastian, M. Le Gallo, R. Khaddam-Aljameh, E. Eleftheriou, *Nature nanotechnology* **2020**, *15*, 7 529.

[29] C. Wu, H. Yu, H. Li, X. Zhang, I. Takeuchi, M. Li, *Acs Photonics* **2018**, *6*, 1 87.

[30] F. Miller, R. Chen, J. E. Fröch, H. Rarick, S. Geiger, A. Majumdar, *Optics Letters* **2023**, *48*, 9 2385.

[31] C. Wu, H. Deng, Y.-S. Huang, H. Yu, I. Takeuchi, C. A. Ríos Ocampo, M. Li, *Science Advances* **2024**, *10*, 1 eadk1361.

[32] W. H. Pernice, H. Bhaskaran, *Applied Physics Letters* **2012**, *101*, 17.

[33] C. Rios, P. Hosseini, C. D. Wright, H. Bhaskaran, W. H. Pernice, *Advanced Materials* **2013**.

[34] C. Williams, N. Hong, M. Julian, S. Borg, H. J. Kim, *Optics Express* **2020**, *28*, 7 10583.

[35] C. C. Popescu, K. Aryana, P. Garud, K. P. Dao, S. Vitale, V. Liberman, H.-B. Bae, T.-W. Lee, M. Kang, K. A. Richardson, et al., *Advanced Materials* **2024**, 2400627.

[36] M. Y. Shalaginov, S. An, Y. Zhang, F. Yang, P. Su, V. Liberman, J. B. Chou, C. M. Roberts, M. Kang, C. Rios, et al., *Nature communications* **2021**, *12*, 1 1225.

[37] W. Jia, R. Menon, B. Sensale-Rodriguez, *Optics Express* **2022**, *30*, 5 6808.

[38] C. Shen, J. Ye, N. Peserico, Y. Gui, C. Dong, H. Kang, B. Movahhed Nouri, H. Wang, E. Heidari, V. J. Sorger, et al., *Nanomaterials* **2023**, *13*, 14 2106.

[39] X. Yin, T. Steinle, L. Huang, T. Taubner, M. Wuttig, T. Zentgraf, H. Giessen, *Light: Science & Applications* **2017**, *6*, 7 e17016.

[40] C. R. de Galarreta, A. M. Alexeev, Y.-Y. Au, M. Lopez-Garcia, M. Klemm, M. Cryan, J. Bertolotti, C. D. Wright, *Advanced Functional Materials* **2018**, *28*, 10 1704993.

[41] M. Zhang, M. Pu, F. Zhang, Y. Guo, Q. He, X. Ma, Y. Huang, X. Li, H. Yu, X. Luo, *Advanced Science* **2018**, *5*, 10 1800835.

[42] C. Ríos, M. Stegmaier, P. Hosseini, D. Wang, T. Scherer, C. D. Wright, H. Bhaskaran, W. H. Pernice, *Nature photonics* **2015**, *9*, 11 725.

[43] W. Zhang, E. Ma, *Materials Today* **2020**, *41* 156.

[44] N. Farmakidis, N. Youngblood, J. S. Lee, J. Feldmann, A. Lodi, X. Li, S. Aggarwal, W. Zhou, L. Bogani, W. H. Pernice, et al., *Advanced Science* **2022**, *9*, 20 2200383.

[45] C. Ríos, Q. Du, Y. Zhang, C.-C. Popescu, M. Y. Shalaginov, P. Miller, C. Roberts, M. Kang, K. A. Richardson, T. Gu, et al., *PhotoniX* **2022**, *3*, 1 26.

[46] Y. Zhang, C. Fowler, J. Liang, B. Azhar, M. Y. Shalaginov, S. Deckoff-Jones, S. An, J. B. Chou, C. M. Roberts, V. Liberman, et al., *Nature Nanotechnology* **2021**, *16*, 6 661.

[47] C.-C. Popescu, B. Mills, L. M. Monier, L. Ranno, Y. Zhang, Q. Du, C. Ríos, S. Vitale, C. Roberts, P. Miller, et al., In *CLEO: Science and Innovations*. Optica Publishing Group, **2023** STh1O–5.

[48] I. Friedrich, V. Weidenhof, W. Njoroge, P. Franz, M. Wuttig, *Journal of applied physics* **2000**, *87*, 9 4130.

[49] K. Aryana, Y. Zhang, J. A. Tomko, M. S. B. Hoque, E. R. Hoglund, D. H. Olson, J. Nag, J. C. Read, C. Ríos, J. Hu, et al., *Nature Communications* **2021**, *12*, 1 1.

[50] Y. Zhang, J. Li, J. Chou, Z. Fang, A. Yadav, H. Lin, Q. Du, J. Michon, Z. Han, Y. Huang, et al., In *CLEO: Science and Innovations*. Optica Publishing Group, **2017** JTh5C–4.

[51] K. Aryana, H. J. Kim, M. R. Islam, N. Hong, C.-C. Popescu, S. Makarem, T. Gu, J. Hu, P. E. Hopkins, *Optical Materials Express* **2023**, *13*, 11 3277.

[52] X. Xu, Q. Zhang, M. Hao, Y. Hu, Z. Lin, L. Peng, T. Wang, X. Ren, C. Wang, Z. Zhao, et al., *Science* **2019**, *363*, 6428 723.

[53] X. Qian, J. Zhou, G. Chen, *Nature Materials* **2021**, 1–15.

[54] A. A. Balandin, S. Ghosh, W. Bao, I. Calizo, D. Teweldebrhan, F. Miao, C. N. Lau, *Nano Letters* **2008**, *8*, 3 902.

[55] D. Ghosh, I. Calizo, D. Teweldebrhan, E. P. Pokatilov, D. L. Nika, A. A. Balandin, W. Bao, F. Miao, C. N. Lau, *Applied Physics Letters* **2008**, *92*, 15 151911.

[56] A. A. Balandin, *Nature Materials* **2011**, *10*, 8 569.

[57] M. Fujii, X. Zhang, H. Xie, H. Ago, K. Takahashi, T. Ikuta, H. Abe, T. Shimizu, *Physical Review Letters* **2005**, *95*, 6 065502.

[58] B. Kumanek, D. Janas, *Journal of Materials Science* **2019**, *54*, 10 7397.

[59] J.-P. Salvetat, J.-M. Bonard, N. Thomson, A. Kulik, L. Forro, W. Benoit, L. Zuppiroli, *Applied Physics A* **1999**, *69*, 3 255.

[60] Z. Ni, H. Bu, M. Zou, H. Yi, K. Bi, Y. Chen, *Physica B: Condensed Matter* **2010**, *405*, 5 1301.

[61] F. P. Incropera, D. P. DeWitt, et al., *Fundamentals of heat and mass transfer*, volume 6, Wiley, **1996**.

[62] A. Giri, P. E. Hopkins, *Advanced Functional Materials* **2020**, *30*, 8 1903857.

[63] M. Wuttig, V. L. Deringer, X. Gonze, C. Bichara, J.-Y. Raty, *Advanced Materials* **2018**, *30*, 51 1803777.

[64] J.-Y. Raty, M. Schumacher, P. Golub, V. L. Deringer, C. Gatti, M. Wuttig, *Advanced Materials* **2019**, *31*, 3 1806280.

[65] C.-F. Schön, S. van Bergerem, C. Mattes, A. Yadav, M. Grohe, L. Kobbelt, M. Wuttig, *Science Advances* **2022**, *8*, 47 eade0828.

[66] H.-K. Lyeo, D. G. Cahill, B.-S. Lee, J. R. Abelson, M.-H. Kwon, K.-B. Kim, S. G. Bishop, B.-k. Cheong, *Applied Physics Letters* **2006**, *89*, 15 151904.

[67] T. Siegrist, P. Jost, H. Volker, M. Woda, P. Merkelbach, C. Schlockermann, M. Wuttig, *Nature materials* **2011**, *10*, 3 202.

[68] J. L. Braun, S. W. King, A. Giri, J. T. Gaskins, M. Sato, T. Fujiseki, H. Fujiwara, P. E. Hopkins, *Applied Physics Letters* **2016**, *109*, 19.

[69] Q. Zheng, S. Li, C. Li, Y. Lv, X. Liu, P. Y. Huang, D. A. Broido, B. Lv, D. G. Cahill, *Advanced Functional Materials* **2018**, *28*, 43 1805116.

[70] C. Chiritescu, D. G. Cahill, N. Nguyen, D. Johnson, A. Bodapati, P. Keblinski, P. Zschack, *Science* **2007**, *315*, 5810 351.

[71] K. Aryana, D. A. Stewart, J. T. Gaskins, J. Nag, J. C. Read, D. H. Olson, M. K. Grobis, P. E. Hopkins, *Nature Communications* **2021**, *12*, 1 2817.

[72] P. B. Allen, J. L. Feldman, *Physical Review B* **1993**, *48*, 17 12581.

[73] D. G. Cahill, R. O. Pohl, *Annual review of physical chemistry* **1988**, *39*, 1 93.

[74] M. T. Agne, R. Hanus, G. J. Snyder, *Energy & Environmental Science* **2018**, *11*, 3 609.

[75] P. B. Allen, J. L. Feldman, J. Fabian, F. Wooten, *Philosophical Magazine B* **1999**, *79*, 11-12 1715.

[76] J. L. Braun, C. H. Baker, A. Giri, M. Elahi, K. Artyushkova, T. E. Beechem, P. M. Norris, Z. C. Leseman, J. T. Gaskins, P. E. Hopkins, *Physical Review B* **2016**, *93*, 14 140201.

[77] H. R. Seyf, A. Henry, *Journal of Applied Physics* **2016**, *120*, 2.

[78] T. Feng, L. Lindsay, X. Ruan, *Physical Review B* **2017**, *96*, 16 161201.

[79] W.-X. Zhou, Y. Cheng, K.-Q. Chen, G. Xie, T. Wang, G. Zhang, *Advanced Functional Materials* **2020**, *30*, 8 1903829.

[80] J.-P. Guin, T. Rouxel, J.-C. Sanglebœuf, I. Melscoët, J. Lucas, *Journal of the American Ceramic Society* **2002**, *85*, 6 1545.

[81] D. G. Cahill, R. Pohl, *Solid State Communications* **1989**, *70*, 10 927.

[82] J. M. Ziman, *Electrons and phonons: the theory of transport phenomena in solids*, Oxford university press, **2001**.

[83] D. G. Cahill, W. K. Ford, K. E. Goodson, G. D. Mahan, A. Majumdar, H. J. Maris, R. Merlin, S. R. Phillpot, *Journal of applied physics* **2003**, *93*, 2 793.

[84] E. Pop, S. Sinha, K. E. Goodson, *Proceedings of the IEEE* **2006**, *94*, 8 1587.

[85] K. Esfarjani, G. Chen, H. T. Stokes, *Physical Review B—Condensed Matter and Materials Physics* **2011**, *84*, 8 085204.

[86] D. G. Cahill, P. V. Braun, G. Chen, D. R. Clarke, S. Fan, K. E. Goodson, P. Keblinski, W. P. King, G. D. Mahan, A. Majumdar, et al., *Applied physics reviews* **2014**, *1*, 1.

[87] T. Chong, L. Shi, R. Zhao, P. Tan, J. Li, H. Lee, X. Miao, A. Du, C. Tung, *Applied physics letters* **2006**, *88*, 12.

[88] S. Raoux, F. Xiong, M. Wuttig, E. Pop, *MRS bulletin* **2014**, *39*, 8 703.

[89] M. Hase, J. Tominaga, *Applied physics letters* **2011**, *99*, 3.

[90] X.-B. Li, N.-K. Chen, X.-P. Wang, H.-B. Sun, *Advanced Functional Materials* **2018**, *28*, 44 1803380.

[91] K. Aryana, H. J. Kim, C.-C. Popescu, S. Vitale, H. B. Bae, T. Lee, T. Gu, J. Hu, *Small* **2023**, *19*, 50 2304145.

[92] C. Kittel, P. McEuen, *Introduction to solid state physics*, John Wiley & Sons, **2018**.

[93] R. Franz, G. Wiedemann, *Annalen der Physik* **1853**, *165*, 8 497.

[94] J. Lee, E. Bozorg-Grayeli, S. Kim, M. Asheghi, H.-S. Philip Wong, K. E. Goodson, *Applied Physics Letters* **2013**, *102*, 19 191911.

[95] W. Zhang, A. Thiess, P. Zalden, R. Zeller, P. Dederichs, J.-Y. Raty, M. Wuttig, S. Blügel, R. Mazzarello, *Nature materials* **2012**, *11*, 11 952.

[96] T. Kato, K. Tanaka, *Japanese journal of applied physics* **2005**, *44*, 10R 7340.

[97] S. Muneer, J. Scoggin, F. Dirisaglik, L. Adnane, A. Cywar, G. Bakan, K. Cil, C. Lam, H. Silva, A. Gokirmak, *AIP Advances* **2018**, *8*, 6 065314.

[98] P. Nukala, R. Agarwal, X. Qian, M. H. Jang, S. Dhara, K. Kumar, A. C. Johnson, J. Li, R. Agarwal, *Nano letters* **2014**, *14*, 4 2201.

[99] T. Nonaka, G. Ohbayashi, Y. Toriumi, Y. Mori, H. Hashimoto, *Thin Solid Films* **2000**, *370*, 1-2 258.

[100] K. Andrikopoulos, S. Yannopoulos, G. Voyiatzis, A. Kolobov, M. Ribes, J. Tominaga, *Journal of physics: condensed matter* **2006**, *18*, 3 965.

[101] J.-W. Park, S. H. Eom, H. Lee, J. L. Da Silva, Y.-S. Kang, T.-Y. Lee, Y. H. Khang, *Physical Review B—Condensed Matter and Materials Physics* **2009**, *80*, 11 115209.

[102] R. O. Jones, *Solid State Sciences* **2024**, *152* 107524.

[103] B.-S. Lee, J. R. Abelson, S. G. Bishop, D.-H. Kang, B.-k. Cheong, K.-B. Kim, *Journal of Applied Physics* **2005**, *97*, 9 093509.

[104] B. Zhang, X.-P. Wang, Z.-J. Shen, X.-B. Li, C.-S. Wang, Y.-J. Chen, J.-X. Li, J.-X. Zhang, Z. Zhang, S.-B. Zhang, et al., *Scientific reports* **2016**, *6*, 1 25453.

[105] R. O. Jones, S. R. Elliott, R. Dronskowski, *Advanced Materials* **2023**, *35*, 30 2300836.

[106] K. Siegert, F. Lange, E. Sittner, H. Volker, C. Schlockermann, T. Siegrist, M. Wuttig, *Reports on Progress in Physics* **2014**, *78*, 1 013001.

[107] K. Aryana, J. T. Gaskins, J. Nag, D. A. Stewart, Z. Bai, S. Mukhopadhyay, J. C. Read, D. H. Olson, E. R. Hoglund, J. M. Howe, et al., *Nature communications* **2021**, *12*, 1 1.

[108] R. Endo, S. Maeda, Y. Jinnai, R. Lan, M. Kuwahara, Y. Kobayashi, M. Susa, *Japanese Journal of Applied Physics* **2010**, *49*, 6R 065802.

[109] K. Cil, F. Dirisaglik, L. Adnane, M. Wennberg, A. King, A. Faraclas, M. B. Akbulut, Y. Zhu, C. Lam, A. Gokirmak, et al., *IEEE Transactions on Electron Devices* **2012**, *60*, 1 433.

[110] L. Crespi, A. Ghetti, M. Boniardi, A. L. Lacaita, *IEEE Electron Device Letters* **2014**, *35*, 7 747.

[111] D. Baratella, D. Dragoni, M. Bernasconi, *Physica Status Solidi (RRL)–Rapid Research Letters* **2022**, 2100470.

[112] V. Bragaglia, F. Arciprete, W. Zhang, A. M. Mio, E. Zallo, K. Perumal, A. Giussani, S. Cecchi, J. E. Boschker, H. Riechert, et al., *Scientific reports* **2016**, *6* 23843.

[113] S. Mukhopadhyay, L. Lindsay, D. J. Singh, *Scientific reports* **2016**, *6* 37076.

[114] D. Campi, L. Paulatto, G. Fugallo, F. Mauri, M. Bernasconi, *Physical Review B* **2017**, *95*, 2 024311.

[115] T. Nirschl, J. Philipp, T. Happ, G. W. Burr, B. Rajendran, M.-H. Lee, A. Schrott, M. Yang, M. Breitwisch, C.-F. Chen, et al., In *2007 IEEE International Electron Devices Meeting*. IEEE, **2007** 461–464.

[116] P. Kapitza, *J Phys USSR* **1941**, *4* 181.

[117] E. T. Swartz, R. O. Pohl, *Reviews of modern physics* **1989**, *61*, 3 605.

[118] J. Chen, X. Xu, J. Zhou, B. Li, *Reviews of Modern Physics* **2022**, *94*, 2 025002.

[119] S. Alosious, S. K. Kannam, S. P. Sathian, B. Todd, *The Journal of chemical physics* **2019**, *151*, 19.

[120] H.-K. Lyeo, D. G. Cahill, *Physical Review B—Condensed Matter and Materials Physics* **2006**, *73*, 14 144301.

[121] C. Hua, X. Chen, N. K. Ravichandran, A. J. Minnich, *Physical Review B* **2017**, *95*, 20 205423.

[122] B. C. Gundrum, D. G. Cahill, R. S. Averback, *Physical Review B—Condensed Matter and Materials Physics* **2005**, *72*, 24 245426.

[123] R. Wilson, D. G. Cahill, *Physical review letters* **2012**, *108*, 25 255901.

[124] C. Monachon, L. Weber, C. Dames, *Annual Review of Materials Research* **2016**, *46*, 1 433.

[125] E.-K. Kim, S.-I. Kwun, S.-M. Lee, H. Seo, J.-G. Yoon, *Applied Physics Letters* **2000**, *76*, 26 3864.

[126] A. Giri, P. E. Hopkins, *Scientific reports* **2017**, *7*, 1 11011.

[127] A. Majumdar, P. Reddy, *Applied Physics Letters* **2004**, *84*, 23 4768.

[128] C. A. Polanco, R. Rastgarkafshgarkolaei, J. Zhang, N. Q. Le, P. M. Norris, A. W. Ghosh, *Physical Review B* **2017**, *95*, 19 195303.

[129] J. P. Reifenberg, D. L. Kencke, K. E. Goodson, *IEEE Electron Device Letters* **2008**, *29*, 10 1112.

[130] J. P. Reifenberg, K.-W. Chang, M. A. Panzer, S. Kim, J. A. Rowlette, M. Asheghi, H.-S. P. Wong, K. E. Goodson, *IEEE Electron Device Letters* **2009**, *31*, 1 56.

[131] S. W. Fong, C. M. Neumann, H.-S. P. Wong, *IEEE Transactions on Electron Devices* **2017**, *64*, 11 4374.

[132] K. Aryana, J. Gaskins, J. Nag, J. Read, D. Olson, M. Grobis, P. Hopkins, *Applied Physics Letters* **2020**, *116*, 4 043502.

[133] E. Bozorg-Grayeli, J. Reifenberg, K. Chang, M. Panzer, K. Goodson, In *2010 12th IEEE Intersociety Conference on Thermal and Thermomechanical Phenomena in Electronic Systems*. IEEE, **2010** 1–7.

[134] M. Jeong, J. P. Freedman, H. J. Liang, C.-M. Chow, V. M. Sokalski, J. A. Bain, J. A. Malen, *Physical Review Applied* **2016**, *5*, 1 014009.

[135] K. Ding, J. Wang, Y. Zhou, H. Tian, L. Lu, R. Mazzarello, C. Jia, W. Zhang, F. Rao, E. Ma, *Science* **2019**, *366*, 6462 210.

[136] J. P. Reifenberg, M. A. Panzer, S. Kim, A. M. Gibby, Y. Zhang, S. Wong, H.-S. P. Wong, E. Pop, K. E. Goodson, *Applied Physics Letters* **2007**, *91*, 11.

[137] J. Wu, M. Breitwisch, S. Kim, T. Hsu, R. Cheek, P. Du, J. Li, E. Lai, Y. Zhu, T. Wang, et al., In *2011 International Electron Devices Meeting*. IEEE, **2011** 3–2.

[138] C. Ahn, S. W. Fong, Y. Kim, S. Lee, A. Sood, C. M. Neumann, M. Asheghi, K. E. Goodson, E. Pop, H.-S. P. Wong, *Nano letters* **2015**, *15*, 10 6809.

[139] C. M. Neumann, K. L. Okabe, E. Yalon, R. W. Grady, H.-S. P. Wong, E. Pop, *Applied Physics Letters* **2019**, *114*, 8.

[140] M. Wuttig, N. Yamada, *Nature materials* **2007**, *6*, 11 824.

[141] B. Gholipour, J. Zhang, K. F. MacDonald, D. W. Hewak, N. I. Zheludev, *Advanced materials* **2013**, *25*, 22 3050.

[142] Q. Wang, E. T. Rogers, B. Gholipour, C.-M. Wang, G. Yuan, J. Teng, N. I. Zheludev, *Nature Photonics* **2016**, *10*, 1 60.

[143] D. Lawson, S. Blundell, M. Ebert, O. L. Muskens, I. Zeimpekis, *Optical Materials Express* **2023**, *14*, 1 22.

[144] S. Nakamura, K. Sekiya, S. Matano, Y. Shimura, Y. Nakade, K. Nakagawa, Y. Monnai, H. Maki, *ACS nano* **2022**, *16*, 2 2690.

[145] P. Garud, K. Aryana, C. C. Popescu, S. Vitale, R. Sharma, K. A. Richardson, T. Gu, J. Hu, H. J. Kim, *physica status solidi (RRL)–Rapid Research Letters* **2024**, 2400177.

[146] C. Wu, S. Brems, D. Yudistira, D. Cott, A. Milenin, K. Vandersmissen, A. Maestre, A. Centeno, A. Zurutuza, J. Van Campenhout, et al., *Laser & Photonics Reviews* **2023**, *17*, 6 2200789.

[147] K.-J. Yoo, D.-Y. Kang, N. Kim, H.-J. Lee, T.-H. Kim, T. Kim, T. G. Kim, *Rare Metals* **2024**, *43*, 1 280.

[148] J. Meng, Y. Gui, B. M. Nouri, X. Ma, Y. Zhang, C.-C. Popescu, M. Kang, M. Miscuglio, N. Peserico, K. Richardson, et al., *Light: Science & Applications* **2023**, *12*, 1 189.

[149] S. Abdollahramezani, O. Hemmatyar, M. Taghinejad, H. Taghinejad, A. Krasnok, A. A. Eftekhar, C. Teichrib, S. Deshmukh, M. A. El-Sayed, E. Pop, et al., *Nature Communications* **2022**, *13*, 1 1696.

[150] Y. Zhang, J. B. Chou, J. Li, H. Li, Q. Du, A. Yadav, S. Zhou, M. Y. Shalaginov, Z. Fang, H. Zhong, et al., *Nature communications* **2019**, *10* 4279.

[151] H. Taghinejad, S. Abdollahramezani, A. A. Eftekhar, T. Fan, A. H. Hosseinnia, O. Hemmatyar, A. E. Dorche, A. Gallmon, A. Adibi, *Optics Express* **2021**, *29*, 13 20449.

[152] J. Zheng, Z. Fang, C. Wu, S. Zhu, P. Xu, J. K. Doylend, S. Deshmukh, E. Pop, S. Dunham, M. Li, et al., *Advanced Materials* **2020**, *32*, 31 2001218.

[153] C. Osburn, Q. Wang, M. Kellam, C. Canovai, P. Smith, G. McGuire, Z. Xiao, G. Rozgonyi, *Applied surface science* **1991**, *53* 291.

[154] S.-L. Zhang, M. Östling, *Critical Reviews in Solid State and Materials Sciences* **2003**, *28*, 1 1.

[155] C. Cabral, K.-N. Chen, L. Krusin-Elbaum, V. Deline, *Applied physics letters* **2007**, *90*, 5.

[156] F. Xiong, M.-H. Bae, Y. Dai, A. D. Liao, A. Behnam, E. A. Carrion, S. Hong, D. Ielmini, E. Pop, *Nano letters* **2013**, *13*, 2 464.

[157] F. Xiong, A. D. Liao, D. Estrada, E. Pop, *Science* **2011**, *332*, 6029 568.

[158] C. Xu, Z. Song, B. Liu, S. Feng, B. Chen, *Applied Physics Letters* **2008**, *92*, 6.

[159] S. Song, Z. Song, C. Peng, L. Gao, Y. Gu, Z. Zhang, Y. Lv, D. Yao, L. Wu, B. Liu, *Nanoscale research letters* **2013**, *8* 1.

[160] F. Rao, Z. Song, Y. Gong, L. Wu, S. Feng, B. Chen, *Nanotechnology* **2008**, *19*, 44 445706.

[161] W. Yang, N. Hur, D.-H. Lim, H. Jeong, J. Suh, *Journal of Applied Physics* **2021**, *129*, 5.

[162] Z. Fang, R. Chen, J. E. Fröch, Q. A. Tanguy, A. I. Khan, X. Wu, V. Tara, A. Manna, D. Sharp, C. Munley, et al., *arXiv preprint arXiv:2307.12103* **2023**.

[163] H. Zhang, L. Zhou, J. Xu, N. Wang, H. Hu, L. Lu, B. Rahman, J. Chen, *Science Bulletin* **2019**, *64*, 11 782.

[164] C.-C. Popescu, K. P. Dao, L. Ranno, B. Mills, L. Martin, Y. Zhang, D. B. Neltner, T. Gu, J. Hu, K. Aryana, et al., *arXiv preprint arXiv:2307.06216* **2023**.

[165] H. Zhang, L. Zhou, L. Lu, J. Xu, N. Wang, H. Hu, B. A. Rahman, Z. Zhou, J. Chen, *ACS Photonics* **2019**, *6*, 9 2205.

[166] K. Kato, M. Kuwahara, H. Kawashima, T. Tsuruoka, H. Tsuda, *Applied Physics Express* **2017**, *10*, 7 072201.

[167] K. S. Novoselov, A. K. Geim, S. V. Morozov, D.-e. Jiang, Y. Zhang, S. V. Dubonos, I. V. Grigorieva, A. A. Firsov, *science* **2004**, *306*, 5696 666.

[168] P. Solís-Fernández, J. Paredes, S. Villar-Rodil, A. Martínez-Alonso, J. Tascón, *Carbon* **2010**, *48*, 9 2657.

[169] C. J. Shearer, A. D. Slattery, A. J. Stapleton, J. G. Shapter, C. T. Gibson, *Nanotechnology* **2016**, *27*, 12 125704.

[170] M. Freitag, M. Steiner, Y. Martin, V. Perebeinos, Z. Chen, J. C. Tsang, P. Avouris, *Nano letters* **2009**, *9*, 5 1883.

[171] W. Cai, A. L. Moore, Y. Zhu, X. Li, S. Chen, L. Shi, R. S. Ruoff, *Nano letters* **2010**, *10*, 5 1645.

[172] J. H. Seol, I. Jo, A. L. Moore, L. Lindsay, Z. H. Aitken, M. T. Pettes, X. Li, Z. Yao, R. Huang, D. Broido, et al., *Science* **2010**, *328*, 5975 213.

[173] D. R. Lide, *CRC handbook of chemistry and physics*, volume 85, CRC press, **2004**.

[174] M. S. Choi, B.-k. Cheong, C. H. Ra, S. Lee, J.-H. Bae, S. Lee, G.-D. Lee, C.-W. Yang, J. Hone, W. J. Yoo, *Advanced Materials* **2017**, *29*, 42 1703568.

[175] X. Tang, S. Xu, J. Zhang, X. Wang, *ACS applied materials & interfaces* **2014**, *6*, 4 2809.

[176] R. Soref, F. De Leonardis, M. De Carlo, V. M. Passaro, *Optics & Laser Technology* **2024**, *176* 111005.

[177] S. Mohammadi-Pouyan, S. Bahadori-Haghighi, A. Rafatmah, B. A. Rahman, *Optics & Laser Technology* **2024**, *169* 110088.

[178] R. R. Ghosh, A. Dhawan, *IEEE Journal of Quantum Electronics* **2023**, *59*, 3 1.

[179] R. Chen, V. Tara, J. Dutta, Z. Fang, J. Zheng, A. Majumdar, *arXiv preprint arXiv:2402.08803* **2024**.

[180] H. Sun, C. Lian, F. Vásquez-Aza, S. R. Kari, Y.-S. Huang, A. Restelli, S. A. Vitale, I. Takeuchi, J. Hu, N. Youngblood, G. Pavlidis, C. A. Ríos Ocampo, Microheater hotspot engineering for repeatable multi-level switching in foundry-processed phase change silicon photonics, **2024**, URL `http://arxiv.org/abs/2407.00059`.

[181] Z. Fang, J. Zheng, A. Saxena, J. Whitehead, Y. Chen, A. Majumdar, *Advanced Optical Materials* **2021**, *9*, 9 2002049.

[182] T. Zhou, Y. Gao, G. Wang, Y. Chen, C. Gu, G. Bai, Y. Shi, X. Shen, *Applied Optics* **2022**, *61*, 7 1660.

[183] J. Xia, Z. Wang, R. Yang, T. Wang, J. Gong, Y. Dong, Z. Li, J. Yao, Q. He, X. Cheng, et al., *Laser & Photonics Reviews* **2024**, *18*, 4 2300722.

[184] J. Gosciniak, *AIP Advances* **2022**, *12*, 3.

[185] J. R. Erickson, V. Shah, Q. Wan, N. Youngblood, F. Xiong, *Optics Express* **2022**, *30*, 8 13673.

[186] A. Shafiee, B. Charbonnier, J. Yao, S. Pasricha, M. Nikdast, *Journal of Optical Microsystems* **2024**, *4*, 3 031208.

[187] C.-Y. Lee, C. Lian, H. Sun, Y.-S. Huang, N. Acharjee, I. Takeuchi, C. A. Ríos Ocampo, *Journal of the American Ceramic Society* **2024**, *107*, 3 1543.

[188] R. E. Simpson, J. K. W. Yang, J. Hu, *Opt. Mater. Express* **2022**, *12*, 6 2368.

[189] M. Stegmaier, C. Rıos, H. Bhaskaran, W. H. Pernice, *Acs Photonics* **2016**, *3*, 5 828.

[190] X. Li, N. Youngblood, C. Ríos, Z. Cheng, C. D. Wright, W. H. Pernice, H. Bhaskaran, *Optica* **2019**, *6*, 1 1.

[191] S. A. Vitale, P. Miller, P. Robinson, C. Roberts, V. Liberman, Q. Du, Y. Zhang, C.-C. Popescu, M. Y. Shalaginov, M. Kang, et al., *Advanced Photonics Research* **2022**, *3*, 10 2200202.

[192] H. Sumikura, T. Wang, P. Li, A.-K. U. Michel, A. Heßler, L. Jung, M. Lewin, M. Wuttig, D. N. Chigrin, T. Taubner, *Nano letters* **2019**, *19*, 4 2549.

[193] J. Zheng, S. Zhu, P. Xu, S. Dunham, A. Majumdar, *ACS applied materials & interfaces* **2020**, *12*, 19 21827.

[194] J. R. Erickson, N. A. Nobile, D. Vaz, G. Vinod, C. A. R. Ocampo, Y. Zhang, J. Hu, S. A. Vitale, F. Xiong, N. Youngblood, *Opt. Mater. Express* **2023**, *13*, 6 1677.

[195] J. D. Musgraves, J. Hu, L. Calvez, editors, *Springer Handbook of Glass*, Springer Handbooks. Springer International Publishing, Cham, **2019**.

[196] Y. Zhang, C. Ríos, M. Y. Shalaginov, M. Li, A. Majumdar, T. Gu, J. Hu, *Applied Physics Letters* **2021**, *118*, 21 210501.

[197] Y. Wang, P. Landreman, D. Schoen, K. Okabe, A. Marshall, U. Celano, H.-S. P. Wong, J. Park, M. L. Brongersma, *Nature Nanotechnology* **2021**, *16*, 6 667.

[198] C. Zhang, M. Wei, J. Zheng, S. Liu, H. Cao, Y. Huang, Y. Tan, M. Zhang, Y. Xie, Z. Yu, et al., *Advanced Optical Materials* **2023**, 2202748.

[199] R. Chen, V. Tara, J. Dutta, Z. Fang, J. Zheng, A. Majumdar, *Journal of Optical Microsystems* **2024**, *4*, 03.

[200] N. Youngblood, C. Talagrand, B. F. Porter, C. G. Galante, S. Kneepkens, G. Triggs, S. Ghazi Sarwat, D. Yarmolich, R. S. Bonilla, P. Hosseini, R. A. Taylor, H. Bhaskaran, *ACS Photonics* **2022**, *9*, 1 90.

[201] R. Chen, V. Tara, M. Choi, J. Dutta, J. Sim, J. Ye, Z. Fang, J. Zheng, A. Majumdar, *npj Nanophotonics* **2024**, *1*, 1 7.

[202] J. Shen, W. Song, K. Ren, Z. Song, P. Zhou, M. Zhu, *Advanced Materials* **2023**, *35*, 11 2208065.

[203] J. Li, Y. Yun, K. Xu, J. Zhang, H. Lin, Y. Zhang, J. Hu, T. Gu, *IEEE Journal of Selected Topics in Quantum Electronics* **2024**, *30*, 4: Adv. Mod. and Int. beyond Si and InP-based Plt. 1.

[204] F. Vasquez-Aza, H. Sun, C. Lian, Y.-s. Huang, S. Vitale, I. Takeuchi, J. Hu, N. Youngblood, C. Rios, G. Pavlidis, In *IEEE Conference on Thermal and Thermomechanical Phenomena in Electronic Systems(ITherm)*. IEEE, Denver, CO, **2024** .

[205] L. Martin-Monier, C. C. Popescu, L. Ranno, B. Mills, S. Geiger, D. Callahan, M. Moebius, J. Hu, *Optical Materials Express* **2022**, *12*, 6 2145.

[206] D. V. Tsu, T. Ohta, *Japanese journal of applied physics* **2006**, *45*, 8R 6294.

[207] H. Lv, P. Zhou, Y. Lin, T. Tang, B. Qiao, Y. Lai, J. Feng, B. Cai, B. Chen, *Microelectronics journal* **2006**, *37*, 9 982.

[208] L. Zhang, B. Park, L. Chapuis, K. Gruel, R. Cours, F. Lorut, M. Hÿtch, C. Gatel, *Journal of Alloys and Compounds* **2024**, *1003* 175626.

[209] K. D. Shukla, N. Saxena, S. Durai, A. Manivannan, *Scientific Reports* **2016**, *6*, 1 37868.

[210] Y. Gutiérrez, S. Dicorato, A. P. Ovvyan, F. Brückerhoff-Plückelmann, J. Resl, M. M. Giangregorio, K. Hingerl, C. Cobet, M. Schiek, M. Duwe, et al., *Advanced Optical Materials* **2024**, *12*, 3 2301564.

[211] D. Tripathi, H. Vyas, S. Kumar, S. S. Panda, R. Hegde, *Nanotechnology* **2023**.

[212] M. Delaney, I. Zeimpekis, D. Lawson, D. W. Hewak, O. L. Muskens, *Advanced Functional Materials* **2020**, *30*, 36 2002447.

[213] N. Youngblood, C. Talagrand, B. F. Porter, C. G. Galante, S. Kneepkens, G. Triggs, S. Ghazi Sarwat, D. Yarmolich, R. S. Bonilla, P. Hosseini, et al., *ACS Photonics* **2021**, *9*, 1 90.

[214] R. Golovchak, J. Plummer, A. Kovalskiy, Y. Holovchak, T. Ignatova, A. Trofe, B. Mahlovanyi, J. Cebulski, P. Krzeminski, Y. Shpotyuk, et al., *Scientific Reports* **2023**, *13*, 1 2881.

[215] M. Zhu, W. Song, P. M. Konze, T. Li, B. Gault, X. Chen, J. Shen, S. Lv, Z. Song, M. Wuttig, et al., *Nature Communications* **2019**, *10*, 1 3525.

[216] M. Salinga, B. Kersting, I. Ronneberger, V. P. Jonnalagadda, X. T. Vu, M. Le Gallo, I. Giannopoulos, O. Cojocaru-Mirédin, R. Mazzarello, A. Sebastian, *Nature materials* **2018**, *17*, 8 681.

[217] R. Simpson, P. Fons, A. Kolobov, T. Fukaya, M. Krbal, T. Yagi, J. Tominaga, *Nature nanotechnology* **2011**, *6*, 8 501.

[218] A. V. Kolobov, P. Fons, Y. Saito, J. Tominaga, *ACS omega* **2017**, *2*, 9 6223.

[219] Y. Saito, M. Morota, K. Makino, J. Tominaga, A. V. Kolobov, P. Fons, *Materials Science in Semiconductor Processing* **2021**, *135* 106079.

[220] P. Prabhathan, K. V. Sreekanth, J. Teng, J. H. Ko, Y. J. Yoo, H.-H. Jeong, Y. Lee, S. Zhang, T. Cao, C.-C. Popescu, et al., *Iscience* **2023**, *26*, 10.

[221] S. Guerin, B. Hayden, D. W. Hewak, C. Vian, *ACS combinatorial science* **2017**, *19*, 7 478.

[222] L. Sun, Y.-X. Zhou, X.-D. Wang, Y.-H. Chen, V. L. Deringer, R. Mazzarello, W. Zhang, *Npj Computational Materials* **2021**, *7*, 1 29.

[223] M. J. Müller, C. Morell, P. Kerres, M. Raghuwanshi, R. Pfeiffer, S. Meyer, C. Stenz, J. Wang, D. N. Chigrin, P. Lucas, M. Wuttig, *Advanced Functional Materials* **2024**, *34*, 39 2403476.

[224] M. Chen, K. A. Rubin, R. Barton, *Applied physics letters* **1986**, *49*, 9 502.

[225] W. K. Njoroge, H.-W. Wöltgens, M. Wuttig, *Journal of Vacuum Science & Technology A: Vacuum, Surfaces, and Films* **2002**, *20*, 1 230.

[226] W. Wełnic, S. Botti, L. Reining, M. Wuttig, *Physical review letters* **2007**, *98*, 23 236403.

[227] K. Konstantinou, T. H. Lee, F. C. Mocanu, S. R. Elliott, *Proceedings of the National Academy of Sciences* **2018**, *115*, 21 5353.

[228] T. H. Lee, S. R. Elliott, *Advanced Materials* **2017**, *29*, 24 1700814.

[229] C. Ciminelli, M. N. Armenise, F. Dell'olio, *Photonics in space: advanced photonic devices and systems*, World Scientific, **2016**.

[230] A. Díaz Fattorini, C. Chèze, I. López García, C. Petrucci, M. Bertelli, F. Righi Riva, S. Prili, S. M. Privitera, M. Buscema, A. Sciuto, et al., *Nanomaterials* **2022**, *12*, 8 1340.

[231] A. Galca, F. Sava, I. Simandan, C. Bucur, V. Dumitru, C. Porosnicu, C. Mihai, A. Velea, *Journal of Non-Crystalline Solids* **2018**, *499* 1.

[232] S. Raoux, H.-Y. Cheng, M. Caldwell, H.-S. Wong, *Applied physics letters* **2009**, *95*, 7.

[233] J. Gainza, F. Serrano-Sanchez, N. Nemes, O. Dura, J. Martinez, J. Alonso, *Materials Today: Proceedings* **2021**, *44*.

[234] J. Zhang, F. Wei, Y. Dong, Z. Shao, Y. Liu, *AIP Advances* **2020**, *10*.

[235] W. Song, L. Shi, X. Miao, T. Chong, *Applied Physics Letters* **2007**, *90*.

[236] J. Hauser, *Physical Review B* **1974**, *9*, 6 2623.

[237] L. Isaenko, A. Yelisseyev, S. Lobanov, V. Petrov, F. Rotermund, J.-J. Zondy, G. Knippels, *Materials science in semiconductor processing* **2001**, *4*, 6 665.

[238] J. Tian, D. Cortecchia, Y. Wang, H. Liu, E. Feltri, H. Liu, G. Adamo, C. Soci, *Nanophotonics* **2022**, *11*, 17 3961.

[239] C. R. de Galarreta, S. G. Carrillo, Y. Au, E. Gemo, L. Trimby, J. Shields, E. Humphreys, J. Faneca, L. Cai, A. Baldycheva, et al., *Journal of Optics* **2020**, *22*, 11 114001.

[240] D. Sahoo, R. Naik, *Materials Research Bulletin* **2022**, *148* 111679.

[241] J.-L. Adam, X. Zhang, *Chalcogenide glasses: preparation, properties and applications*, Woodhead publishing, **2014**.

[242] R. Wang, F. R. Lange, S. Cecchi, M. Hanke, M. Wuttig, R. Calarco, *Advanced functional materials* **2018**, *28*, 14 1705901.

[243] K. L. Okabe, A. Sood, E. Yalon, C. M. Neumann, M. Asheghi, E. Pop, K. E. Goodson, H.-S. P. Wong, *Journal of Applied Physics* **2019**, *125*, 18.

[244] J. Tominaga, S. Sumi, H. Awano, *Applied Physics Express* **2020**, *13*, 7 075503.

[245] B.-Q. Wang, T.-Y. Zhao, H.-R. Ding, Y.-T. Liu, N.-K. Chen, M. Niu, X.-D. Li, M. Xu, H.-B. Sun, S. Zhang, et al., *Acta Materialia* **2024**, 120123.

[246] C. Wang, J. Zhai, Z. Song, X. Yao, *Japanese Journal of Applied Physics* **2009**, *48*.

[247] B. Gholipour, S. R. Elliot, M. J. Muller, M. Wuttig, D. W. Hewak, B. E. Hayden, S. S. Jo, R. Jaramillo, R. E. Simplson, *Journal of Physics: Photonics* **2023**, *5*.

[248] Y. Saito, Y. Sutou, P. Fons, S. Shindo, X. Kozina, J. M. Skelton, A. V. Kolobov, K. Kobayashi, *Chemistry of Materials* **2017**, *29*, 17 7440.

[249] Y. Li, A. Singh, S. Krylyuk, A. Davydov, R. Jaramillo, In *Low-Dimensional Materials and Devices 2019*, volume 11085. SPIE, **2019** 32–39.

[250] S. Irfan, Y. A. Haleem, M. I. Irshad, M. F. Saleem, M. Arshad, M. Habib, *Optics* **2023**, *4*, 2 351.

[251] A. Singh, Y. Li, B. Fodor, L. Makai, J. Zhou, H. Xu, A. Akey, J. Li, R. Jaramillo, *Applied Physics Letters* **2019**, *115*, 16.

[252] S. Sun, X. Wang, Y. Jiang, Y. Lei, S. Zhang, S. Kumar, J. Zhang, E. Ma, R. Mazzarello, J.-J. Wang, W. Zhang, *npj computational materials* **2024**, *10*.

[253] N. Yamada, E. Ohno, K. Nishiuchi, N. Akahira, M. Takao, *Journal of Applied Physics* **1991**, *69*, 5 2849.

[254] J. Zhao, J. Hui, Z. Ye, T. Lai, M. Y. Efremov, H. Wang, L. H. Allen, *Advanced Materials Interfaces* **2022**, *9*, 23 2200429.

[255] M. H. Lankhorst, B. W. Ketelaars, R. A. Wolters, *Nature materials* **2005**, *4*, 4 347.

[256] S. Raoux, B. Muñoz, H.-Y. Cheng, J. L. Jordan-Sweet, *Applied Physics Letters* **2009**, *95*, 14.

[257] G. C. Sosso, J. Behler, M. Bernasconi, *physica status solidi (b)* **2012**, *249*, 10 1880.

[258] J. Akola, R. Jones, *Physical Review B* **2007**, *76*, 23 235201.

[259] K. Ghosh, A. Kusiak, P. Noé, M.-C. Cyrille, J.-L. Battaglia, *Physical Review B* **2020**, *101*, 21 214305.

[260] E. Levin, M. Besser, R. Hanus, *Journal of Applied Physics* **2013**, *114*, 8.

[261] P. Bauer Pereira, I. Sergueev, S. Gorsse, J. Dadda, E. Müller, R. P. Hermann, *physica status solidi (b)* **2013**, *250*, 7 1300.

[262] R. J. Warzoha, B. F. Donovan, N. T. Vu, J. G. Champlain, S. Mack, L. B. Ruppalt, *Applied Physics Letters* **2019**, *115*, 2.

[263] Y. Zhou, M. Leng, Z. Xia, J. Zhong, H. Song, X. Liu, B. Yang, J. Zhang, J. Chen, K. Zhou, et al., *Advanced energy materials* **2014**, *4*, 8.

[264] A. Pashinkin, A. Malkova, M. Mikhailova, *Russian Journal of Physical Chemistry A, Focus on Chemistry* **2008**, *82* 1035.

[265] K. Zeng, D.-J. Xue, J. Tang, *Semiconductor Science and Technology* **2016**, *31*, 6 063001.

[266] R. Kondrotas, C. Chen, J. Tang, *Joule* **2018**, *2*, 5 857.

[267] M. A. Popescu, *Non-Crystalline Chalcogenicides*, volume 8, Springer Science & Business Media, **2001**.

[268] V. Gurevich, K. Gavrichev, V. Gorbunov, E. Busheva, L. Golushina, G. Bergman, *Geochemistry International* **2002**, *40*, 2 164.

[269] T. B. Nasr, H. Maghraoui-Meherzi, N. Kamoun-Turki, *Journal of Alloys and Compounds* **2016**, *663* 123.

[270] S. Meng, J. Wang, H. Shi, X. Sun, B. Gao, *Physical Chemistry Chemical Physics* **2021**.

[271] Y. Ma, M. Liu, A. Jasber, R. Y. Wang, *Journal of Materials Chemistry A* **2015**, *3*.

[272] A. e. a. Waghmare, *Journal of Solid State Electrochemistry* **2022**, *26*.

[273] M. Alzhdanov, M. Nadzhafzade, Z. Seidov, *Physics of the Solid State* **1999**, *41*.

[274] W. Wang, Z. Wu, D. Yang, Y. Zhao, T. Cheng, *Optical and Quantum Electronics* **2023**, *55*.

[275] I. McGieson, V. Bird, C. Barr, K. Hattar, B. Reed, J. McKeown, F. Yi, D. LaVan, M. Santala, *Optical and Materials Research* **2022**, *37*.

[276] K. Ding, B. Chen, Y. Chen, J. Wang, X. Shen, F. Rao, *npg Asia Materials* **2020**, *12*, 63.

[277] H. Kwon, A. I. Khan, C. Perez, M. Asheghi, E. Pop, K. E. Goodson, Uncovering thermal and electrical properties of sb2te3/gete superlattice films, **2021**.

[278] S. Raoux, G. W. Burr, M. J. Breitwisch, C. T. Rettner, Y.-C. Chen, R. M. Shelby, M. Salinga, D. Krebs, S.-H. Chen, H.-L. Lung, et al., *IBM Journal of Research and Development* **2008**, *52*, 4.5 465.

[279] M. Y. Shalaginov, S. D. Campbell, S. An, Y. Zhang, C. Ríos, E. B. Whiting, Y. Wu, L. Kang, B. Zheng, C. Fowler, et al., *Nanophotonics* **2020**, *9*, 11 3505.

[280] G. W. Burr, M. J. Breitwisch, M. Franceschini, D. Garetto, K. Gopalakrishnan, B. Jackson, B. Kurdi, C. Lam, L. A. Lastras, A. Padilla, et al., *Journal of Vacuum Science & Technology B* **2010**, *28*, 2 223.

[281] D. Turnbull, *Contemporary physics* **1969**, *10*, 5 473.

[282] J. Kalb, M. Wuttig, F. Spaepen, *Journal of materials research* **2007**, *22*, 3 748.

[283] C. Persch, M. J. Müller, A. Yadav, J. Pries, N. Honné, P. Kerres, S. Wei, H. Tanaka, P. Fantini, E. Varesi, et al., *Nature communications* **2021**, *12*, 1 4978.

[284] H. J. Kim, J.-w. Sohn, N. Hong, C. Williams, W. Humphreys, *Journal of Physics: Photonics* **2021**, *3*, 2 024008.

[285] N. A. Nobile, J. R. Erickson, C. Ríos, Y. Zhang, J. Hu, S. A. Vitale, F. Xiong, N. Youngblood, *ACS photonics* **2023**, *10*, 10 3576.

[286] A. Redaelli, A. Pirovano, A. Benvenuti, A. L. Lacaita, *Journal of Applied Physics* **2008**, *103*, 11 6.

[287] S. Caravati, M. Bernasconi, T. Kühne, M. Krack, M. Parrinello, *Applied Physics Letters* **2007**, *91*, 17.

[288] J. Kalikka, J. Akola, R. Jones, *Physical Review B* **2014**, *90*, 18 184109.

[289] J. Y. Raty, W. Zhang, J. Luckas, C. Chen, R. Mazzarello, C. Bichara, M. Wuttig, *Nature communications* **2015**, *6*, 1 7467.

[290] B. J. Kooi, M. Wuttig, *Advanced Materials* **2020**, *32*, 21 1908302.

[291] V. S. A. Varri, D. Tripathi, H. S. Vyas, P. Agarwal, R. S. Hegde, *Optical Materials Express* **2021**, *11*, 4 988.

[292] V. L. Deringer, M. A. Caro, G. Csányi, *Advanced Materials* **2019**, *31*, 46 1902765.

[293] Y. Zhou, W. Zhang, E. Ma, V. L. Deringer, *Nature Electronics* **2023**, *6*, 10 746.

[294] M. Le Gallo, A. Sebastian, *Journal of Physics D: Applied Physics* **2020**, *53*, 21 213002.

[295] S. Zhuo, Y. Li, A. Zhao, Y.-R. Li, S. Yao, M. Zhang, T. Feng, Z. Li, *Laser & Photonics Reviews* **2023**, *17*, 1 2200403.

[296] K. P. Dao, J. Hu, *Journal of Applied Physics* **2024**, *136*, 22.

[297] I.-M. Park, J.-K. Jung, S.-O. Ryu, K.-J. Choi, B.-G. Yu, Y.-B. Park, S. M. Han, Y.-C. Joo, *Thin Solid Films* **2008**, *517*, 2 848.

[298] H. Zhang, X. Yang, J. Chen, B. Rahman, L. Zhou, et al., *Optics Express* **2021**, *29*, 3 3503.

[299] A. Faraclas, N. Williams, A. Gokirmak, H. Silva, *IEEE electron device letters* **2011**, *32*, 12 1737.

[300] G. W. Burr, P. Tchoulfian, T. Topuria, C. Nyffeler, K. Virwani, A. Padilla, R. M. Shelby, M. Eskandari, B. Jackson, B.-S. Lee, *Journal of Applied Physics* **2012**, *111*, 10.

[301] Z. Woods, A. Gokirmak, *IEEE Transactions on Electron Devices* **2017**, *64*, 11 4466.

[302] Z. Woods, J. Scoggin, A. Cywar, A. Gokirmak, et al., *IEEE Transactions on Electron Devices* **2017**, *64*, 11 4472.

[303] Y. Li, F. Liu, G. Han, Q. Chen, Y. Zhang, X. Xie, L. Zhang, Y. Lian, *Nanotechnology* **2021**, *32*, 40 405201.

[304] R. Zhao, H. Tong, X. Miao, *physica status solidi (RRL)–Rapid Research Letters* **2023**, *17*, 8 2200463.